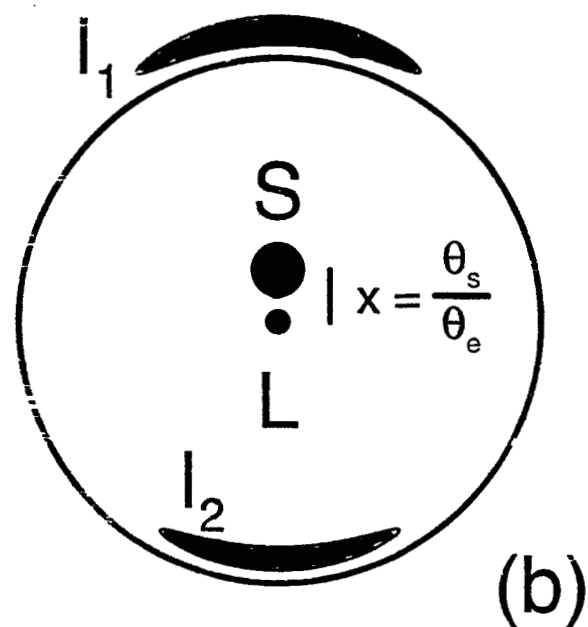
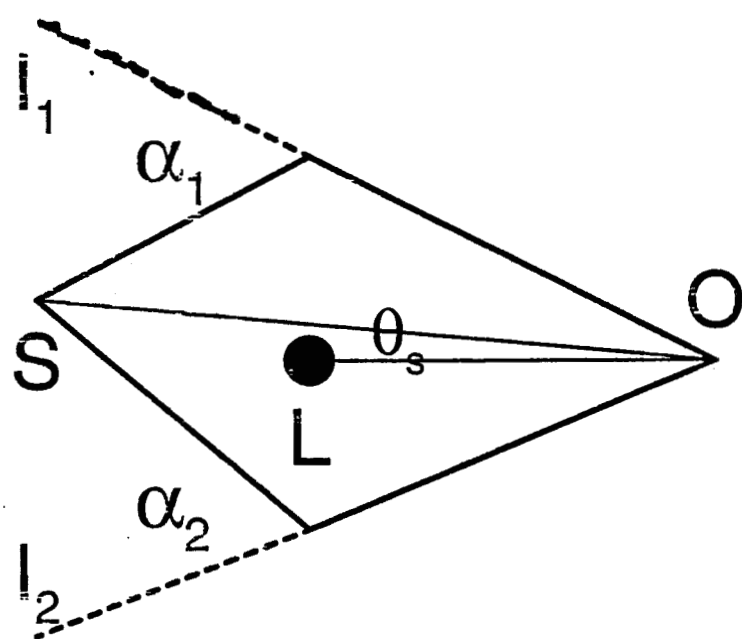
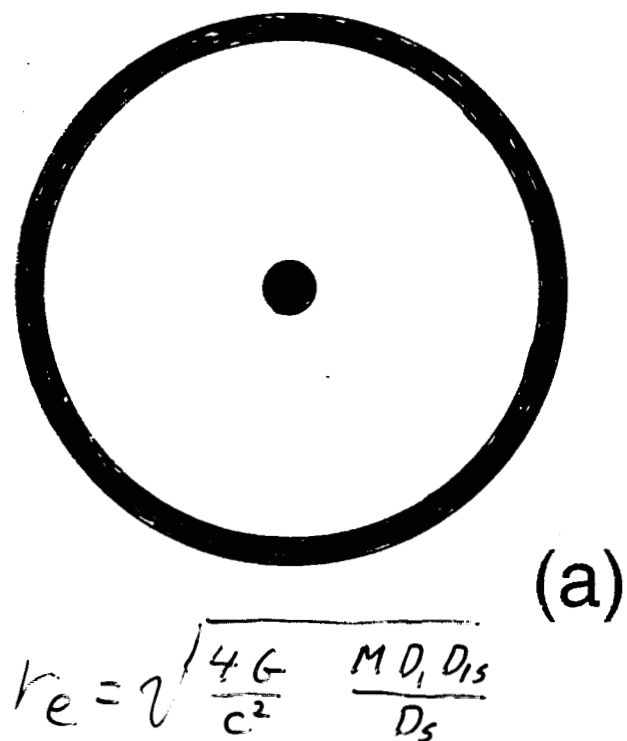
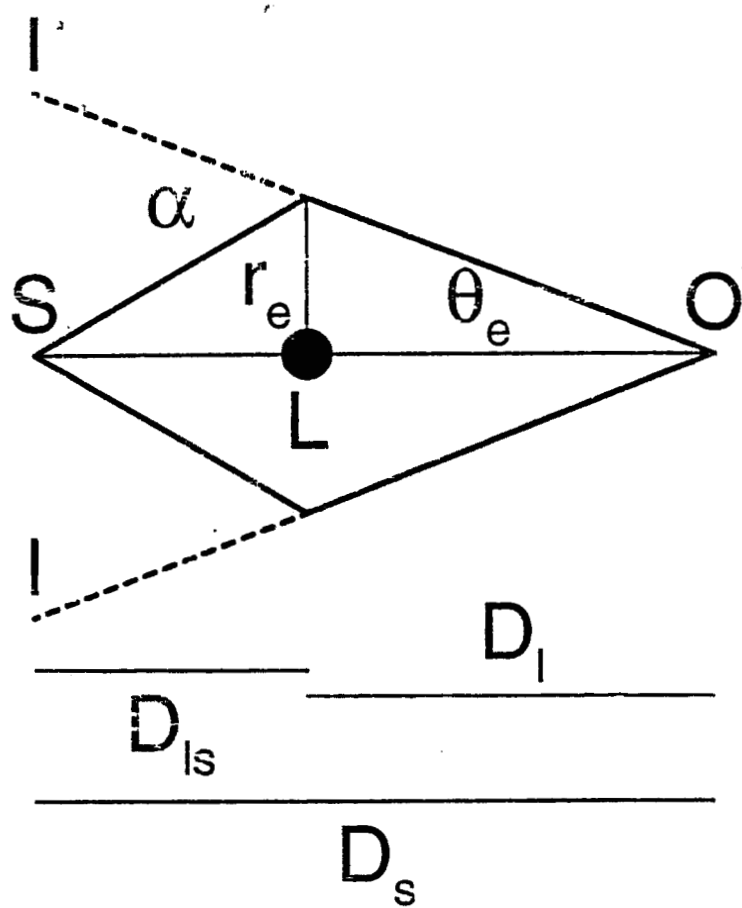


ASTROMETRIC MICROLENSING

ANDY GOULD

OHIO
STATE
UNIVERSITY



$$A(x) = \frac{\text{arc} + \text{arc}}{\bullet} = \frac{x^2 + 2}{x(x^2 + 4)^{1/2}}$$

(c)

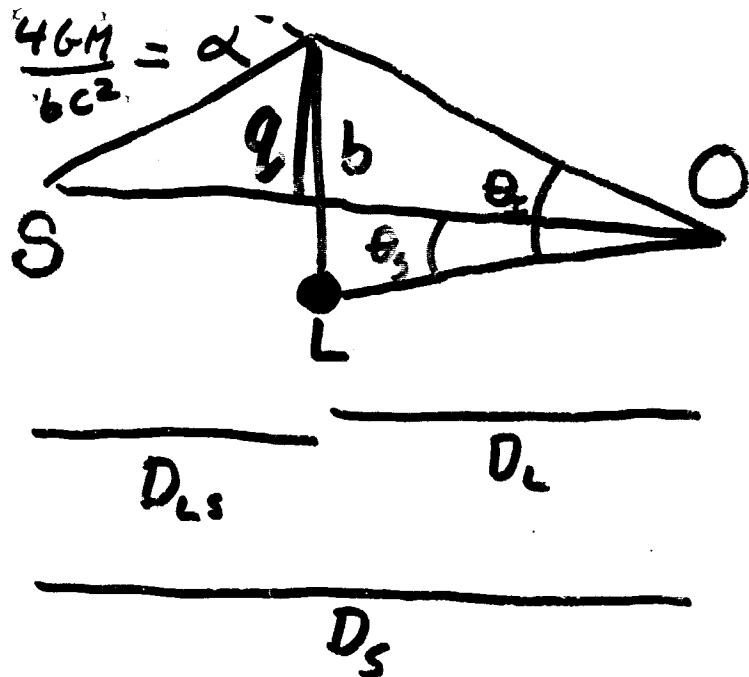


IMAGE POSITIONS
 $\pm u_{\pm}$

$$\frac{q}{D_{LS}} + \frac{q}{D_L} = \alpha = \frac{4GM}{bc^2}$$

$$\frac{4GM D_{LS} D_L}{c^2 (D_{LS} + D_L)} = qb = (\theta_I - \theta_s) D_L \theta_I D_L$$

$$\theta_E^2 \equiv \frac{4GM D_{LS}}{c^2 D_S D_L} = \theta_I^2 - \theta_I \theta_s$$

$$u \equiv \frac{\theta_s}{\theta_E}$$

$$\frac{\theta_I}{\theta_E} = \pm u_{\pm}$$

$$u_{\pm} \equiv \frac{\sqrt{u^2 + 4} \pm u}{2}$$

MAGNIFICATIONS A_{\pm}

JACOBIAN: $\vec{u} \rightarrow \pm u_{\pm} \hat{u}$

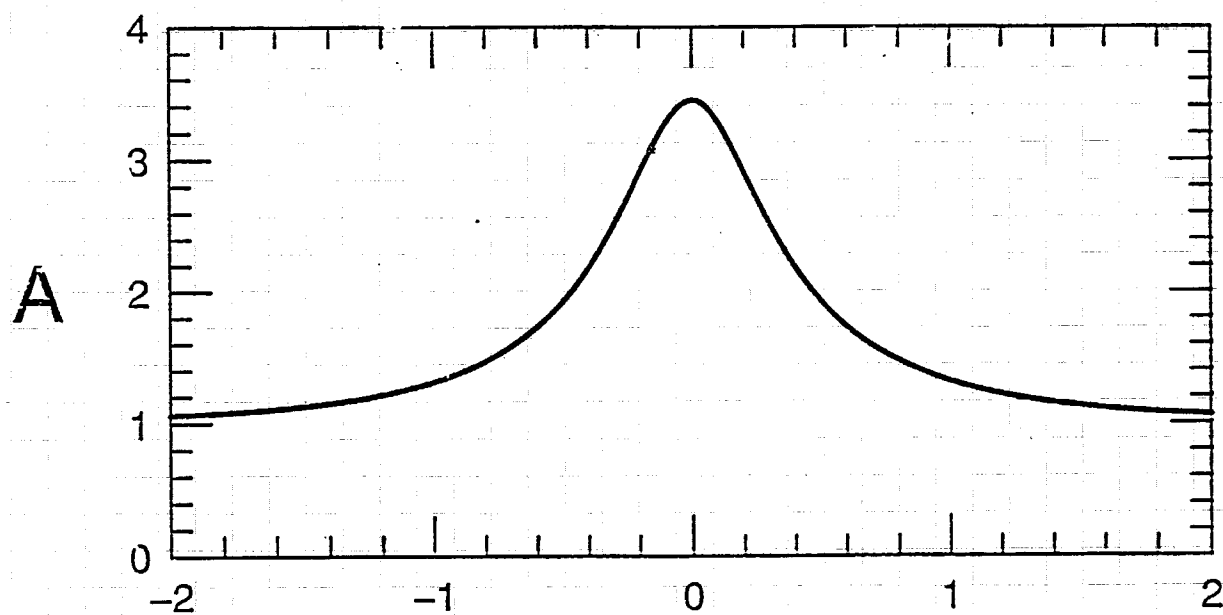
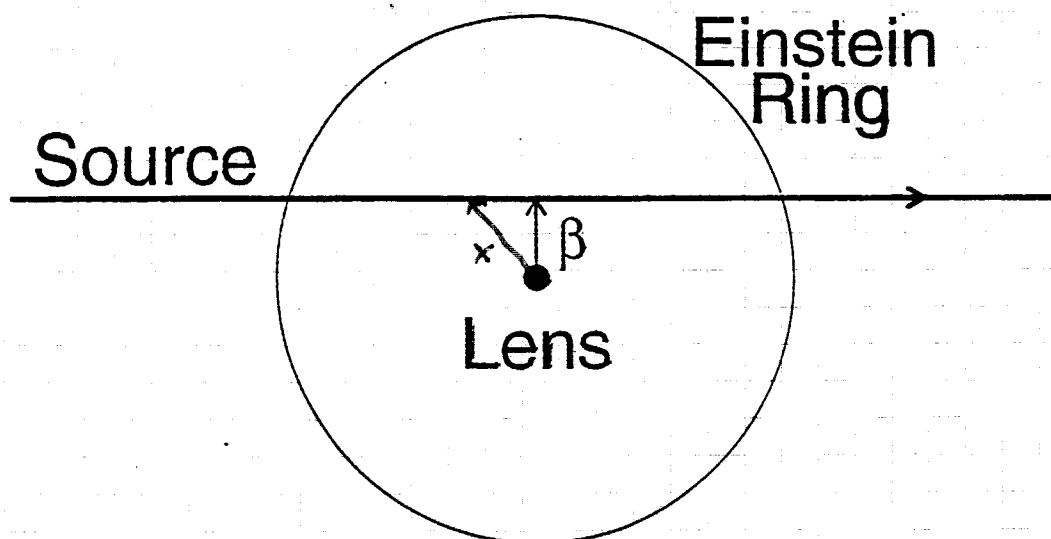
$$A_{\pm} = \frac{u_{\pm}}{u} \frac{du_{\pm}}{du} = \frac{u_{\pm}^2}{u_{+}^2 - u_{-}^2}$$

CENTROID

$$u_c = u_{+} A_{+} - u_{-} A_{-}$$

$$= \frac{u_{+}^3 - u_{-}^3}{u_{+}^2 - u_{-}^2} = u + \frac{u}{u^2 + 2}$$

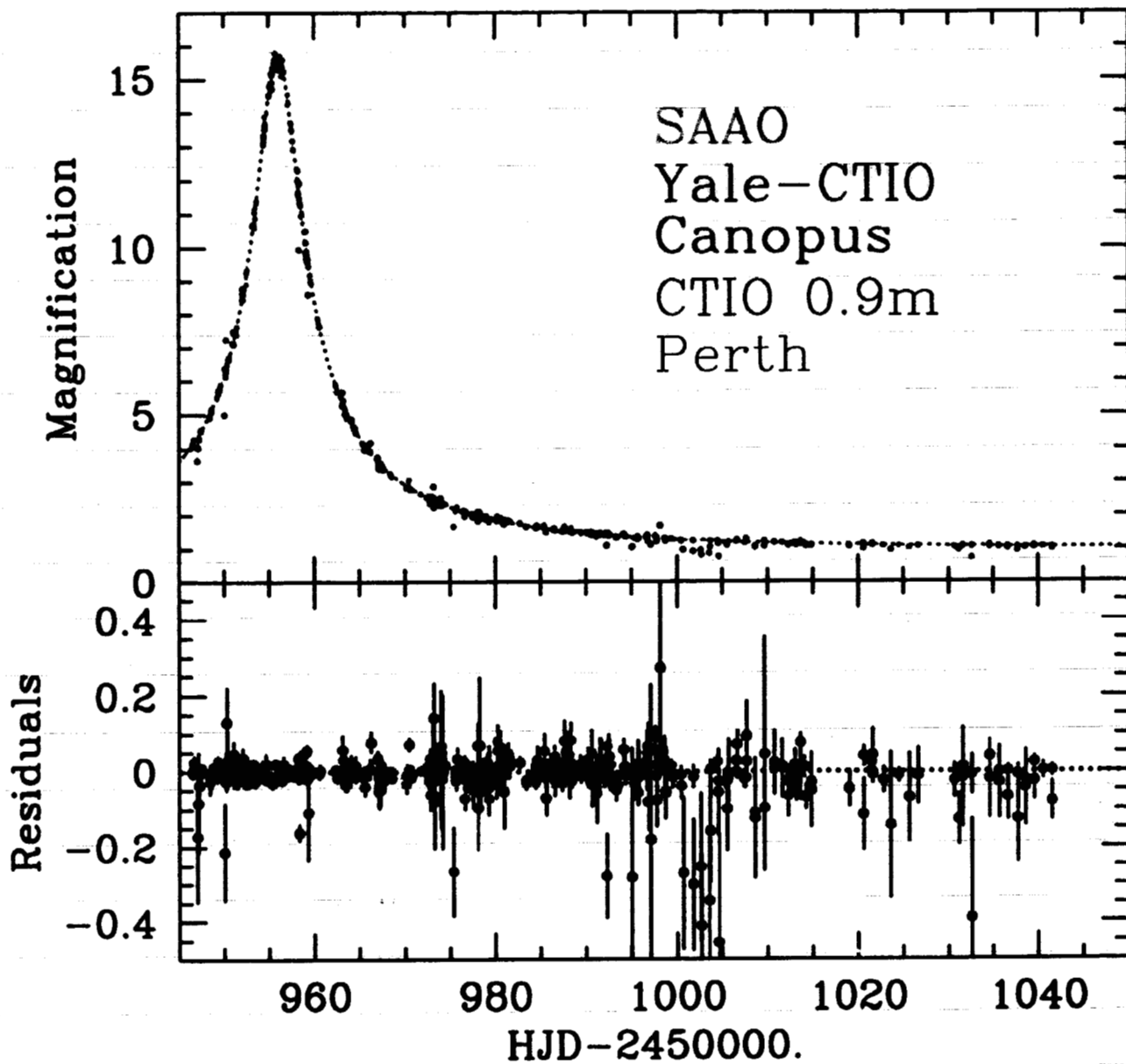
$$\Delta \vec{u}_c = \vec{u}_c - \vec{u} = \frac{\vec{u}}{u^2 + 2}$$



$$A[x(t)] : \quad x(t) = \sqrt{\frac{(t - t_0)^2}{t_e^2} + \beta^2}$$

Limits on Companions: OGLE-1998-BUL-14

Albrow et al. (2000)



Micro Lensing Observables

LENS

SOURCE

π_l D_l
 $\vec{\mu}_l$ or $\vec{V}_{l,\perp}$

STRUCTURE
MASS

π_s D_s
 $\vec{\mu}_s$ or $\vec{V}_{s,\perp}$
 V_r

STRUCTURE

$\pi_l, \vec{\mu}_l, M, \pi_s, \vec{\mu}_s$

$$\frac{\alpha}{\tilde{r}_E} = \frac{\theta_E}{r_E} \Rightarrow$$

$$\theta_E \tilde{r}_E = \alpha r_E = \frac{4G}{c^2} M$$

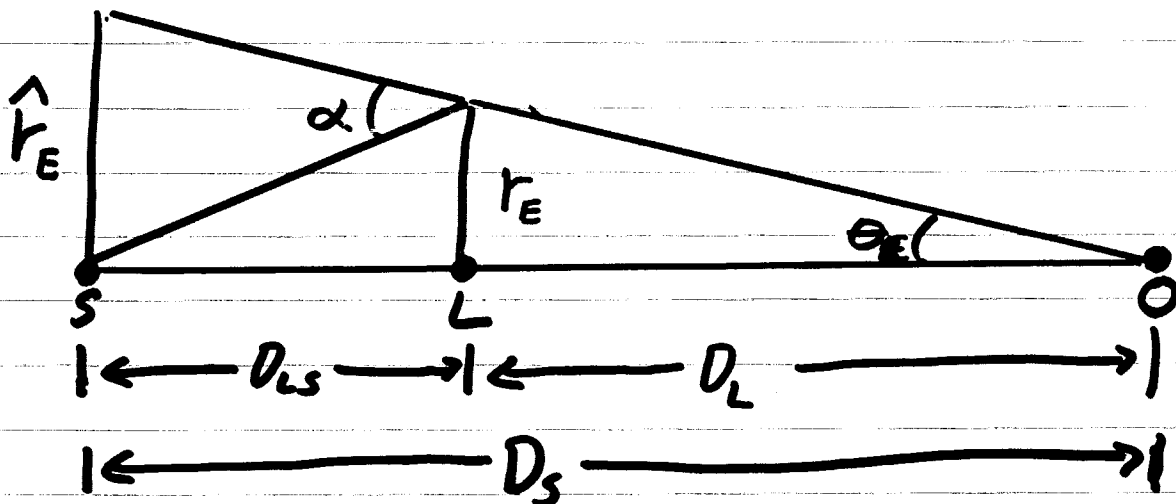
| r_E

$$\theta_E = \alpha - \psi = \frac{\tilde{r}_E}{D_L} - \frac{\tilde{r}_E}{D_S} = \frac{\tilde{r}_E}{D_{rel}}$$

$$\frac{1}{D_{rel}} \equiv \frac{1}{D_L} - \frac{1}{D_S}$$

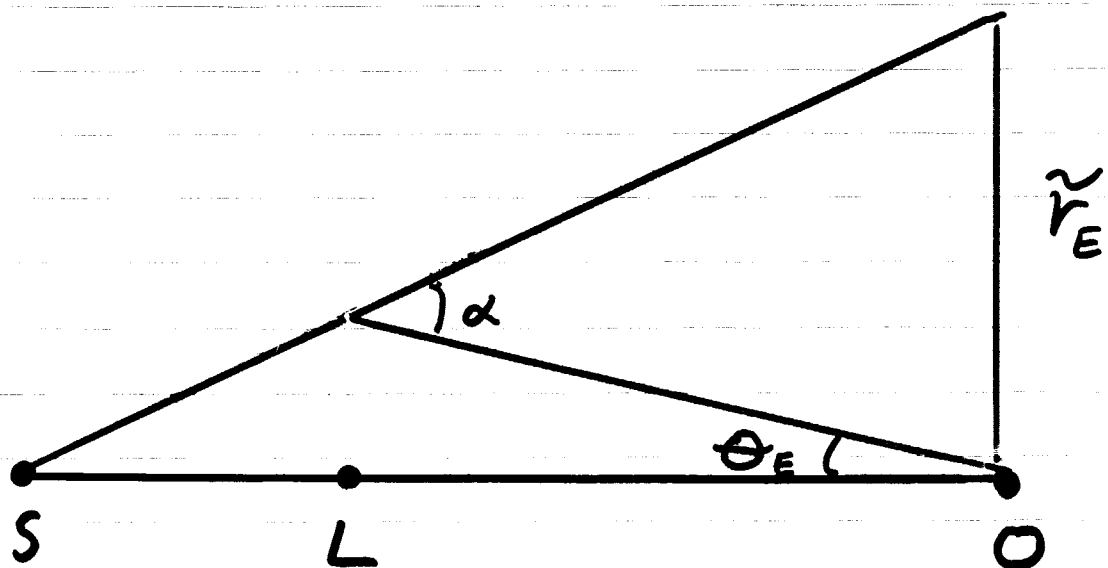
14

Standard Picture



EINSTEIN: $\alpha = \frac{4GM}{c^2 r_E}$

Natural Picture



$$\Theta_E \tilde{r}_E = \frac{4GM}{c^2}$$

$$\frac{\tilde{r}_E}{\Theta_E} = D_{rel}$$

$$\Theta_E = \sqrt{\frac{4GM}{c^2} \frac{1}{D_{rel}}}$$

$$\tilde{r}_E = \sqrt{\frac{4GM}{c^2} D_{rel}}$$

$$D_{rel} = \frac{D_L D_S}{D_{LS}}$$

$$\frac{1}{D_{rel}} = \frac{1}{D_L} - \frac{1}{D_S}$$

$$\frac{AU}{D_{rel}} \equiv \pi_{rel} = \pi_L - \pi_S \Rightarrow \pi_{rel} = \pi_E \Theta_E$$

$$\pi_E \equiv \frac{AU}{\tilde{r}_E}$$

$$\pi_{rel} = \pi_E \Theta_E$$

$$\vec{\mu}_{rel} = \vec{\mu}_L - \vec{\mu}_S$$

$$\epsilon_E = \frac{\Theta_E}{|\vec{\mu}_{rel}|} = \frac{\Theta_E}{\mu_{rel}}$$

$$\mu_E \equiv \frac{1}{\epsilon_E}$$

$$\vec{\mu}_E = \frac{\vec{\mu}_{rel}}{\Theta_E}$$

Measurable Quantities

SOURCE: $\pi_s, \vec{\mu}_s$

EVENT: $\theta_E, \tilde{r}_E, \tau_E, \phi$

$\theta_E, \vec{\pi}_E, \mu_E$

$\theta_E, \pi_E, \vec{\mu}_E$

LENS:

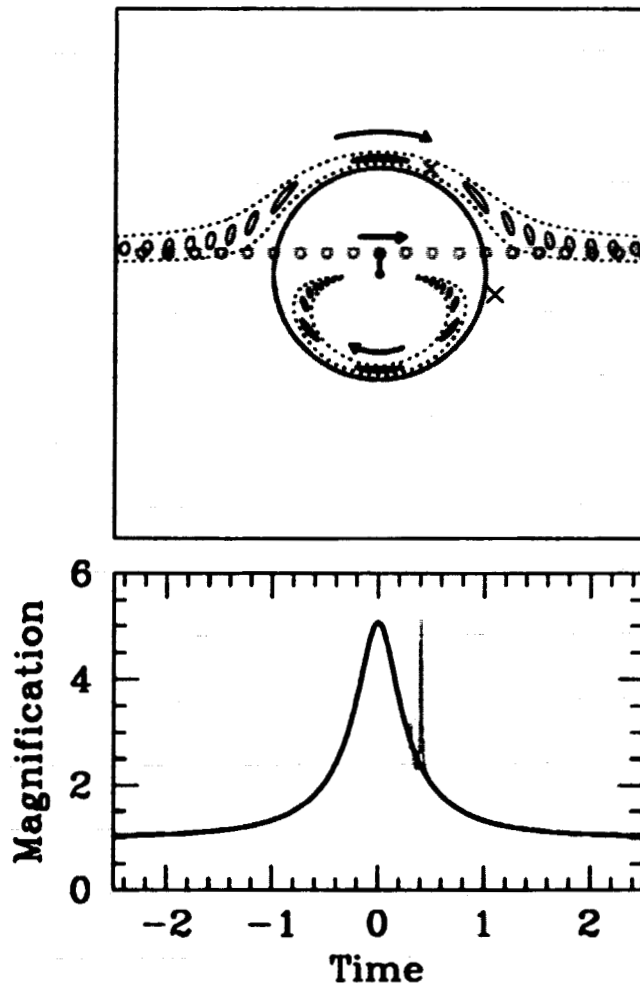
$$M = \frac{c^2 AU}{4G} \frac{\theta_E}{\pi_E}$$

$$\pi_L = \pi_s + \pi_E \theta_E$$

$$\vec{\mu}_L = \vec{\mu}_s + \vec{\mu}_E \theta_E$$

$$\vec{V}_L = \frac{\vec{\mu}_s + \vec{\mu}_E \theta_E}{\pi_s + \pi_E \theta_E} AU$$

Planetary Microlensing



Einstein Ring Crossing Time:

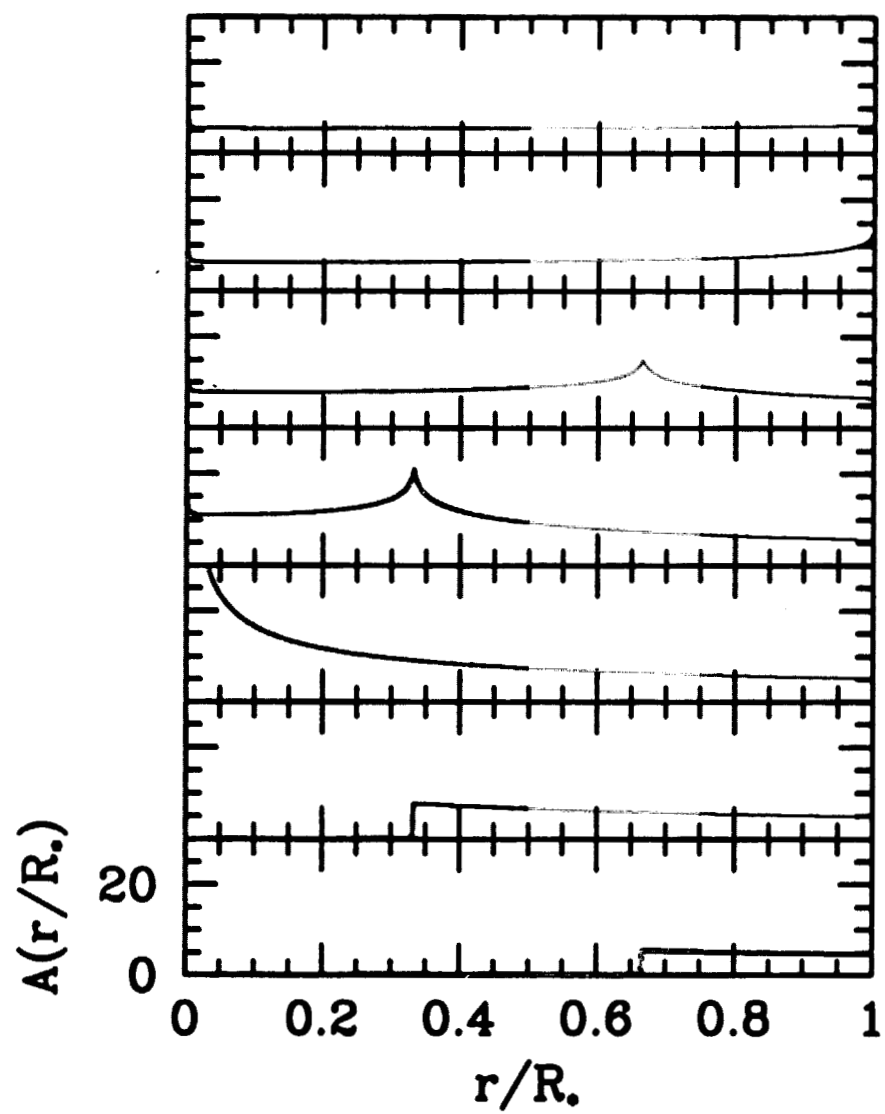
$$t_E = \frac{\theta_E}{\mu} \simeq 20 \text{ days} \left(\frac{M}{0.3M_\odot} \right)^{1/2} \left(\frac{v}{150 \text{ km s}^{-1}} \right)^{-1}$$

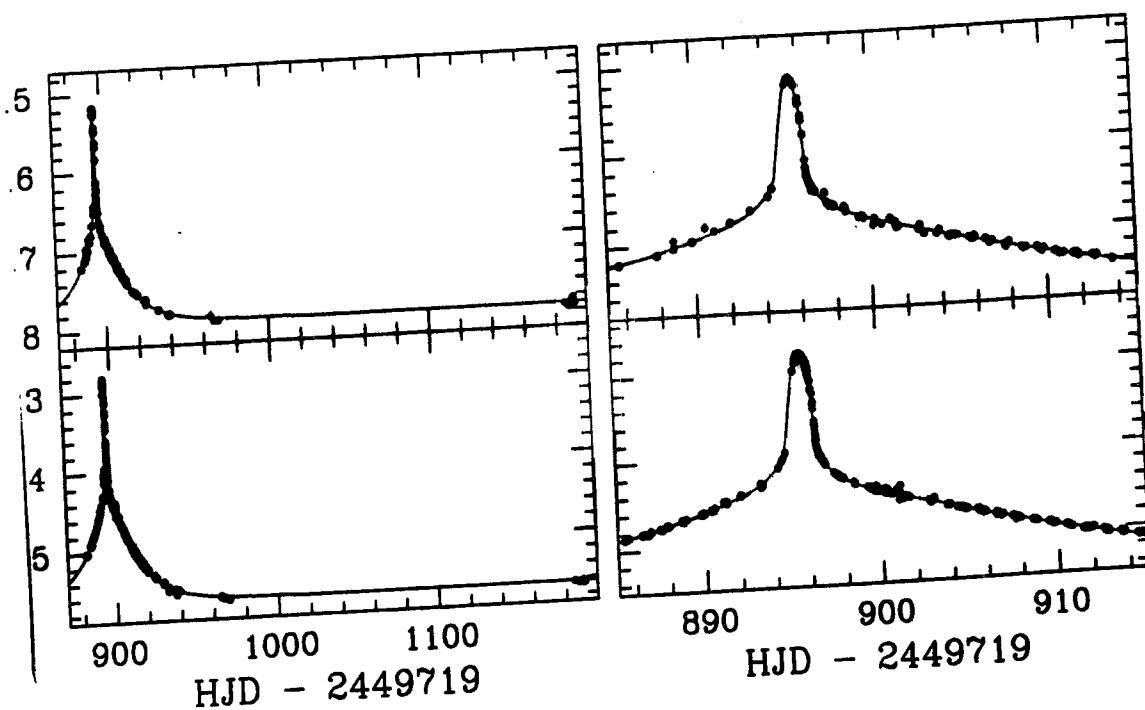
Perturbation Timescale:

$$t_p \sim q^{1/2} t_E$$

Parameters

$$q, b, \theta$$





3. 1.—*Left*: High-quality subset of PLANET photometry for γ -G-28 spanning a 300 day period and consisting of 431 *I*-band points (*m*) and 155 *V*-band points (*top*) from three PLANET observing stations in Tasmania, Chile, and South Africa, shown with baseline points the following season. Light curves for our best-fitting limb-darkened 1 (LD2) are superimposed. *Right*: An enlargement showing the 30 day

2, 1999

PLANET PHOTOMETRY OF MACHO 97-BLG-28

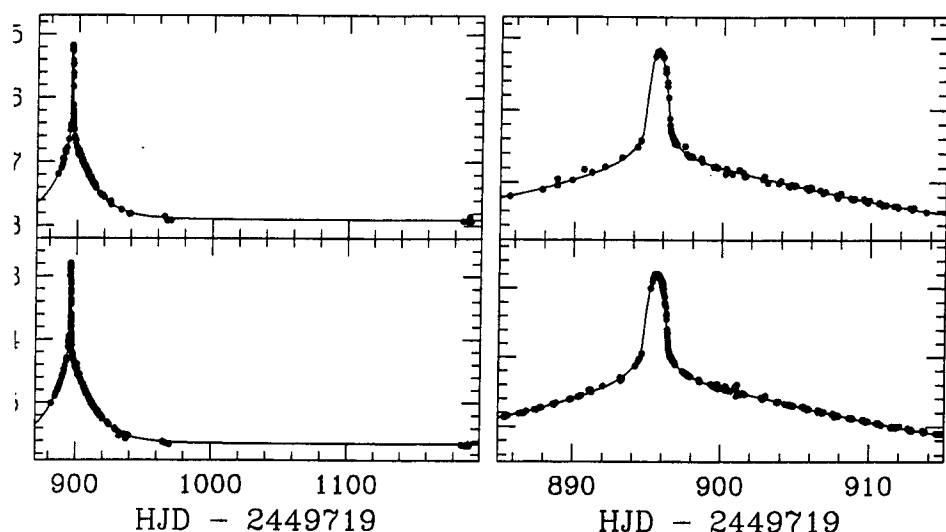


FIG. 1.—*Left*: High-quality subset of PLANET photometry for G-28 spanning a 300 day period and consisting of 431 *I*-band points (bottom) and 155 *V*-band points (top) from three PLANET observing stations: Tasmania, Chile, and South Africa, shown with baseline points from the following season. Light curves for our best-fitting limb-darkened (LD2) are superimposed. *Right*: An enlargement showing the 30 day near the peak.

Measurements that deviated by 0.75 mag for constant as bright as $I = 14$ was also excluded. This highly subset of our data¹³ consists of 586 data points (431 *I*-band: 247 La Silla, 130 SAAO, 54 Tasmania; and 155 *V*-band: 98 La Silla, 41 SAAO, 16 Tasmania) and is displayed in Figure 1.

2.2. Spectroscopy

On 1997 May 31, prior to the anomalous peak of MACHO 97-BLG-28, red and blue spectra were taken of the source star by M. Sahu using the high-throughput FOCES (ESO Faint Object Spectrographic Camera) on the 3.6 m telescope at La Silla, Chile. The camera has both imaging and spectroscopic capabilities, and can hold five spectrographs simultaneously so that multiple spectral

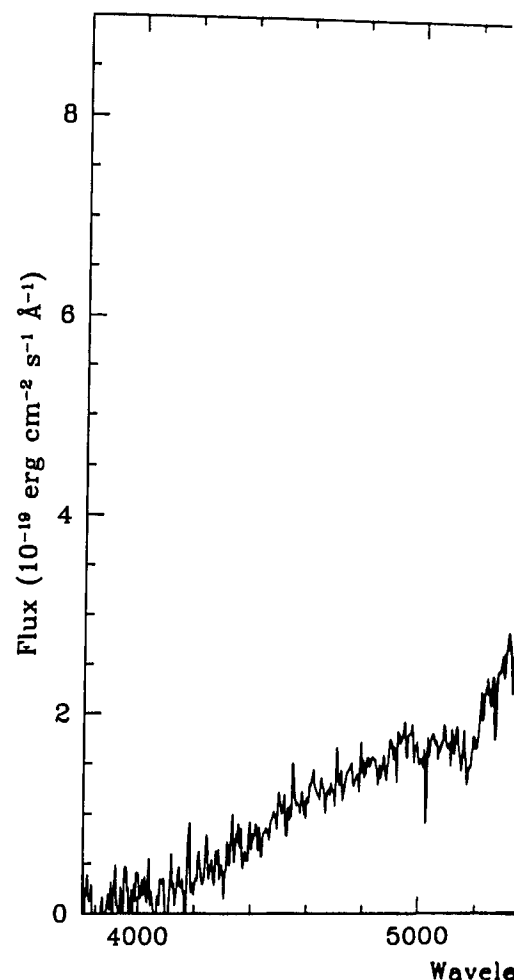


FIG. 2.—Flux-calibrated combined EFOSC on the ESO 3.6 m. The spectrum was taken before the anomalous peak was magnified.

resolution of about 260 km s⁻¹ resolution feature near 5890 Å. The b resolution velocities is 9.5 km s⁻¹, which resolution of the spectrum.

2.3. Radius and Spectra

Comparison of the flux cal

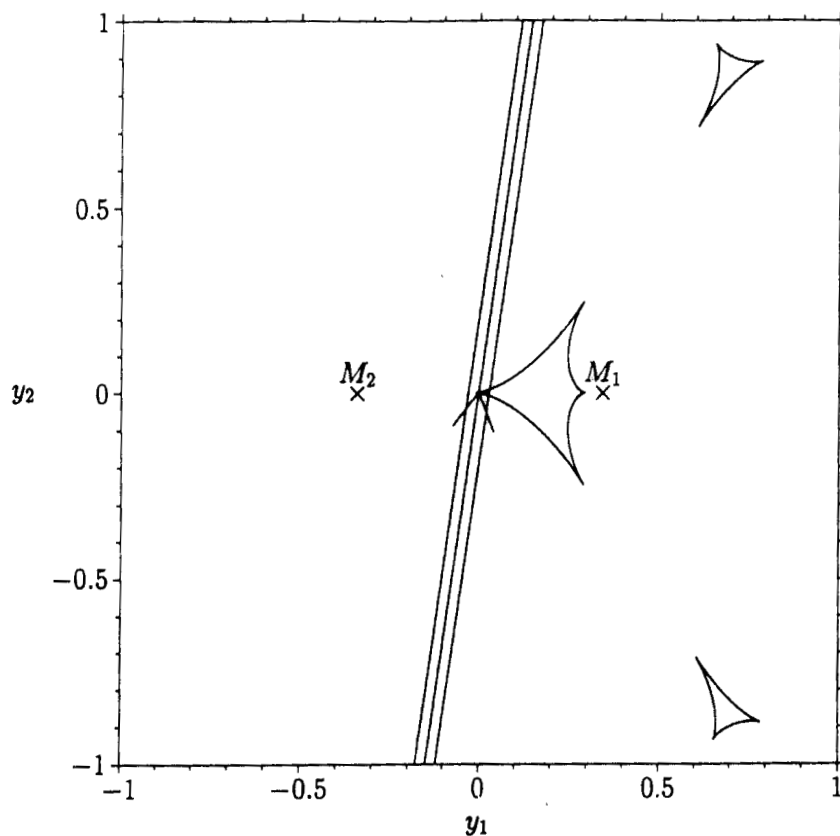


FIG. 5.—Configuration of binary lens and trajectory of the extended source on the sky from the two-parameter limb-darkening model. The lens caustics are shown as the closed, pointed shapes in the center and at the right side of the diagram. The path of the source is indicated by the straight parallel lines; the distance between the two outer parallel lines corresponds to the source width. Lens positions are shown as crosses; M_1 is the heavier of the two. All distances are in units of the angular Einstein radius.

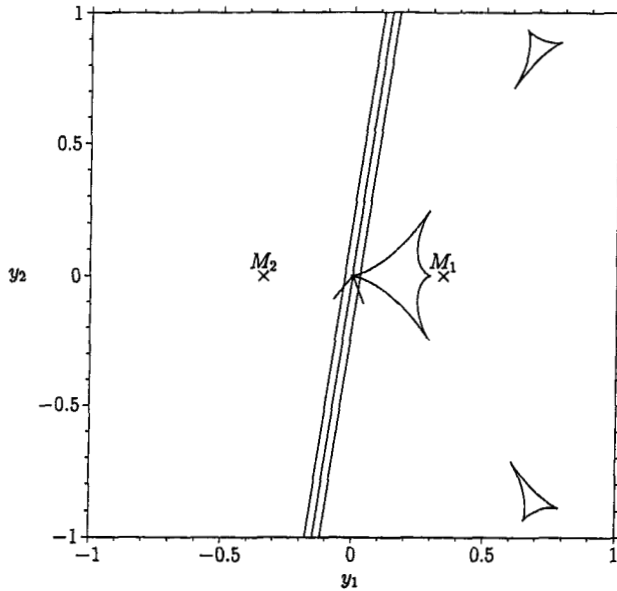


FIG. 5.—Configuration of binary lens and trajectory of the extended source on the sky from the two-parameter limb-darkening model. The lens caustics are shown as the closed, pointed shapes in the center and at the right side of the diagram. The path of the source is indicated by the straight parallel lines; the distance between the two outer parallel lines corresponds to the source width. Lens positions are shown as crosses; M_1 is the heavier of the two. All distances are in units of the angular Einstein radius.

Dominik (1998). The multisite, multiband baselines were allowed to vary independently in the fitting process; this photometric alignment resulted in relative multisite offsets of 0.007–0.065 mag in our best model.

In general, it is a difficult task to find a minimum in a high dimensional parameter space. However, in this case, nearly optimal values for some parameters could be found by first searching in lower dimensional subspaces. The six baselines could be estimated from the latest data points and then fitted with a point-lens model together with the parameters u_0 , t_0 , t_E , and the two blending parameters, using the data points outside the peak region. We thus began fitting the binary-lens extended-source models only after we had good guesses for 11 of the parameters. Parameters from the uniform-source fit then provided us with good initial estimates for a total of 15 parameters, requiring only two or four additional parameters when including limb darkening.

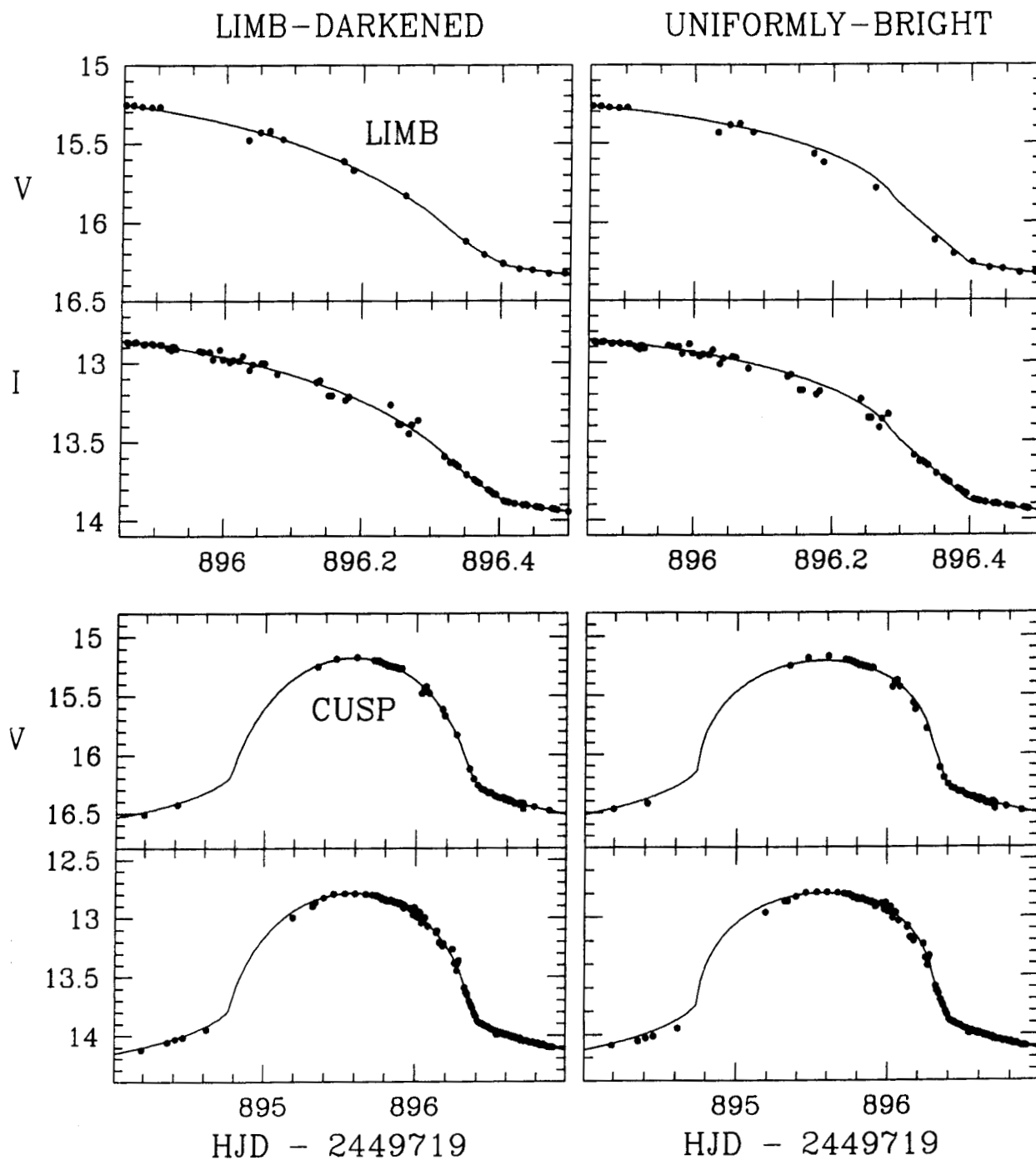
Our best fit was achieved for a two-parameter limb-darkening model (LD2), and yielded a χ^2_{\min} of 1913 for the 567 degrees of freedom (dof). This model is displayed in the left panels of Figure 4, and its fit parameters are listed in Table 1. If the LD2 model is indeed the best representation of the data, then the reduced $\chi^2_{\min}/\text{dof} = 3.374$ is an indication that the DoPHOT uncertainties are on average underestimated by a factor of ~ 1.8 , consistent with our previous experience (Albrow et al. 1998).

The corresponding source trajectory and caustic struc-

TABLE 1
PLANET MODEL PARAMETERS FOR GALACTIC BULGE EVENT MACHO 97-BLG-28

PARAMETER	FORMAL DOPHOT ERROR BARS			FRAME-QUALITY ERROR BARS		
	LD2	LD1	UB	LD2	LD1	UB
χ^2_{\min}	1913	1930	3255	264	281	450
Number of dof	567	569	571	667	669	671
Number of parameters	19	17	15	19	17	15
t_E (days)	27.3	27.2	26.1	27.3	27.3	26.1
t_0 (days)	895.58	895.58	895.63	895.58	895.58	895.63
u_0	0.0029	0.0030	0.021	0.0029	0.0034	0.021
d	0.686	0.687	0.678	0.686	0.688	0.680
q	0.234	0.232	0.277	0.234	0.231	0.276
α	1.426	1.424	1.406	1.427	1.422	1.419
f_I	0.97	0.98	0.98	0.97	0.98	0.96
f_V	0.84	0.84	0.85	0.85	0.88	0.87
ρ_*	0.0286	0.0287	0.0296	0.0286	0.0289	0.0295
c_I	0.40	0.75	0	0.38	0.83	0
c_V	0.55	0.92	0	0.55	0.95	0
d_I	0.37	0	0	0.38	0	0
d_V	0.44	0	0	0.43	0	0
m_0^L	15.632	15.633	15.620	15.630	15.631	15.597
m_0^S	15.643	15.644	15.631	15.643	15.645	15.609
m_0^T	15.708	15.703	15.727	15.697	15.697	15.673
m_0^V	17.899	17.898	17.889	17.909	17.930	17.900
m_0^{SV}	17.906	17.905	17.903	17.914	17.938	17.903
m_0^{TV}	17.926	17.918	17.965	17.947	17.959	17.968

NOTE.—Listed are the model parameters for two-parameter limb-darkened (LD2), one-parameter limb-darkened (LD1), and uniformly bright (UB) source models. The first three columns indicate fits of high-quality data with DoPHOT-reported error bars; the last three columns list fits of all data with empirical “frame quality” uncertainties, based on typical scatter for similar brightness stars on individual frames. The baselines m_0 refer to the total modeled flux (source + blend) at the given observing site (L = LaSilla, S = SAAO, T = Tasmania) and in the given band (I or V).



Left: Light curves for our best fit, the two-parameter limb-darkening model (LD2), superimposed on PLANET V and I data sets for a 3 day period on the cusp-crossing (bottom) and a 16 hr period during which the stellar limb swept over the cusp (top). Right: The same, but for the uniform brightness model (UB). DoPHOT estimates for relative photometric uncertainties have been assumed; the rescaled error bars are generally comparable to the plotted points, and so have been omitted.

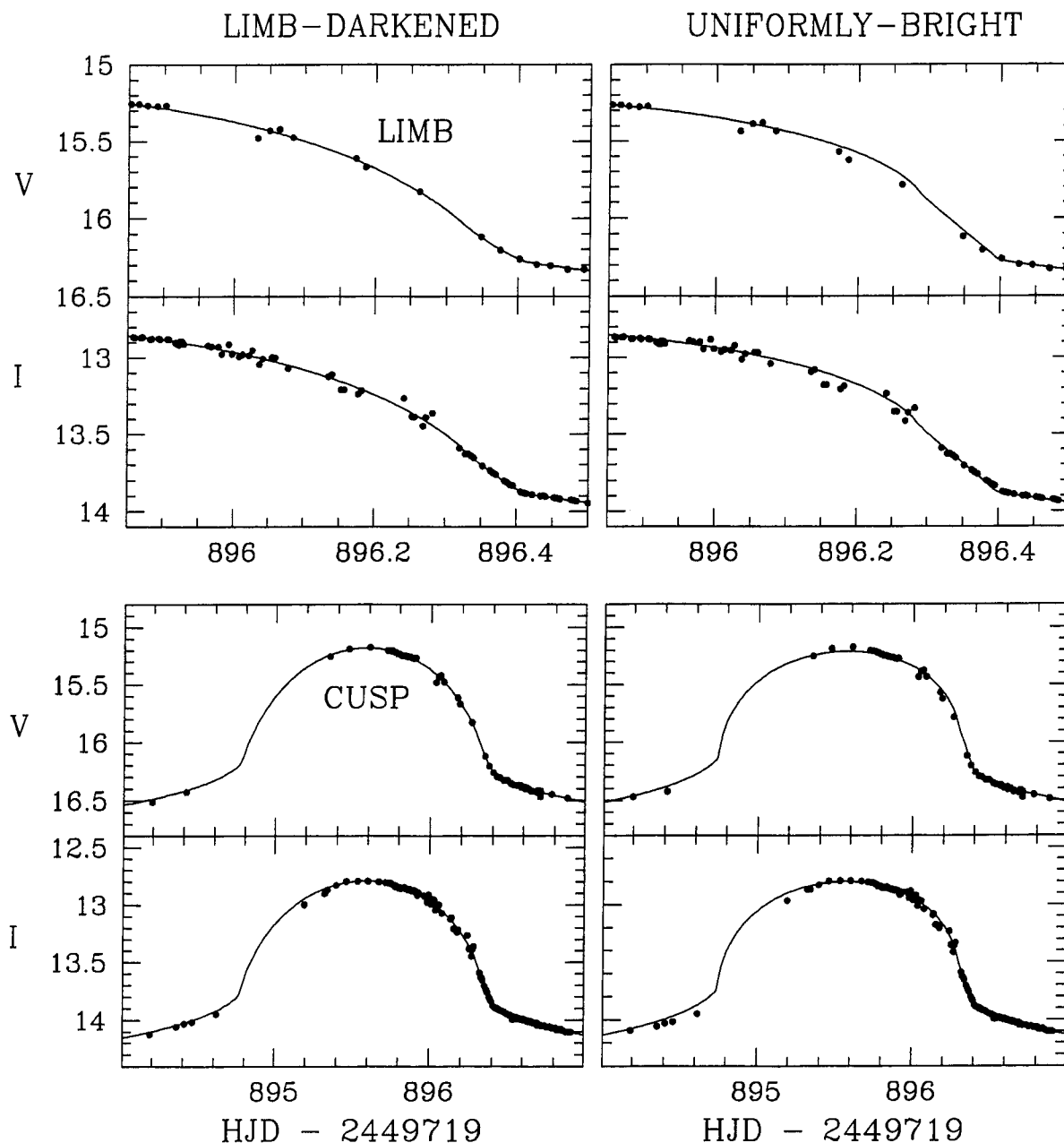


FIG. 4.—*Left*: Light curves for our best fit, the two-parameter limb-darkening model (LD2), superimposed on PLANET V and I data sets for a 3 day period centered on the cusp-crossing (*bottom*) and a 16 hr period during which the stellar limb swept over the cusp (*top*). *Right*: The same, but for the uniform bright source model (UB). DoPHOT estimates for relative photometric uncertainties have been assumed; the rescaled error bars are generally comparable to the size of the plotted points, and so have been omitted.

extended size of the source is characterized by an additional parameter, $\rho_* \equiv \theta_*/\theta_E$, the angular radius of the source in units of the Einstein radius. Finally, the light-intensity profile of the source may be limb darkened rather than uniform over the stellar disk. We adopt a limb-darkening law of the form

$$I_\lambda(\mathcal{G}) = I_\lambda(0)[1 - c_\lambda(1 - \cos \mathcal{G}) - d_\lambda(1 - \sqrt{\cos \mathcal{G}})], \quad (2)$$

where \mathcal{G} is the angle between the normal to the stellar surface and the line of sight. The coefficients c_λ and d_λ are wavelength dependent, requiring an additional $2n$ parameters.

The inclusion of all these effects thus requires $7 + k + 3n$ fit parameters. For the three PLANET sites, each observing MACHO 97-BLG-28 in V and I , $k = 6$ and $n = 2$, thus necessitating 19 parameters in the full model.

3.1. Fitting the Model to the Data

We fit three different extended-source binary-lens models, with either a uniform source or a one- or two-parameter limb-darkened source, to the combined high-quality data set of 586 CCD frames (§ 2.1) using the formal uncertainties reported by DoPHOT. Details of calculating the light curves for such models can be found in the work of

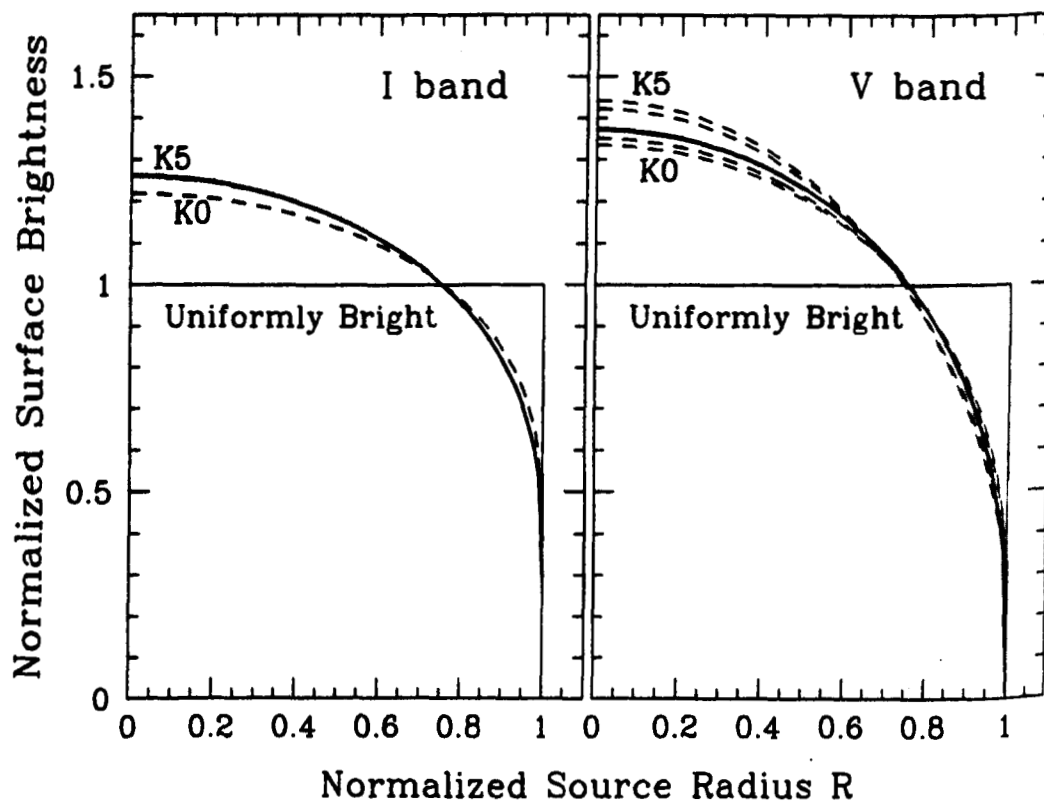


FIG. 8.—Source radial profiles in the *I*-band (left) and *V*-band (right) for uniformly bright (thin solid line) and our two-parameter limb-darkened source (thick solid line) models. Also shown are the theoretical expectations in the Cousins *I* and Johnson *V*-bands based on atmospheric models for K0–K5 giants (dashed lines) from two different literature sources (see text).

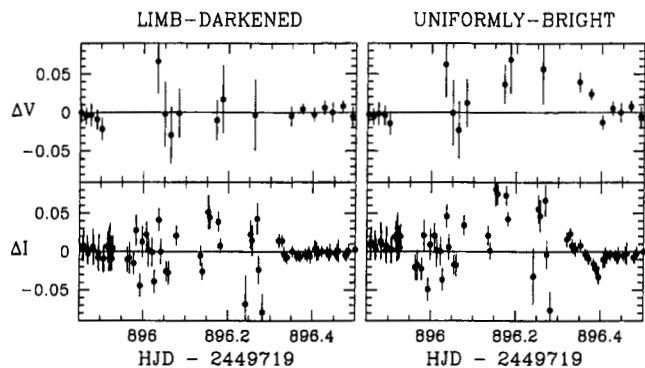


FIG. 7.— V - and I -band residuals (model-data) for the models of Fig. 4 during the brief period in which the cusp swept over the trailing limb of the source. (Rescaled) formal DoPHOT error bars are shown. The different sampling rates and observing conditions at the three sites (successively La Silla, Tasmania, and SAAO) is apparent. *Left*: Residuals for our best-fitting two-parameter limb-darkening model (LD2). *Right*: The same, but for the uniformly bright source model (UB).

significance of the LD2 model over the LD1 model is thus determined by the 8.2% probability of obtaining by chance a $\Delta\chi^2_{\min} > 5$ improvement with 2 additional degrees of freedom, corresponding to a marginal 1.7σ detection of a surface profile that deviates from the one-parameter limb-darkening law in both bands. This marginal improvement indicates that the inclusion of additional profile-fitting parameters beyond those included in the LD2 model is unlikely to result in a significantly better fit; the LD2 model contains all the information that we are able to pull from this data set about the source profile.

The large difference in $\Delta\chi^2_{\min}$ between the limb-darkened and uniform bright models is not due solely to the cuspcrossing portions of the light curve. Since the model parameters are correlated, even those parameters unrelated to the source profile differ between the uniform source model and the limb-darkened models, as inspection of Table 1 indicates. Interestingly, the limb-darkened models always required a smaller photometric offset between sites in both bands. The uniform-brightness model apparently attempted to match the observed shape of the light curve at the limb by adjusting the photometric offsets slightly, hindering the χ^2 performance of the UB model elsewhere in the light curve. The clear signature of limb darkening is revealed only with high-precision data during the few hours when the limb of the star is grazing the caustic; high-quality data over the whole of the light curve is required, however, to obtain a full and accurate microlensing solution.

4.1. Robustness of the Measurement

Another test of the reliability of our limb-darkening parameters is provided by fits we performed on the full data set, including the poorer quality frames, but now estimating the photometric uncertainties empirically, so that the size of the error bar scales with the overall frame quality. Specifically, we set the uncertainty of the event magnitude on a given frame to be equal to the average deviation of all similarly bright constant stars from their average magnitude. We also eliminated the baseline points taken in 1998 in order to test whether the availability of a long temporal baseline was important to our conclusions about limb darkening. The resulting χ^2_{\min} and fit parameters are given in the last three columns of Table 1 for the three source

models. The value of χ^2_{\min} now appears to be too small, primarily due to the fact that 97-BLG-28 is less crowded than a typical star of its brightness, so that the frame-quality uncertainties are overestimates of its true photometric scatter. What is important to note is that the uniformly bright source is again strongly ruled out and that all model parameters are left almost entirely unaffected by this alternate selection and treatment of the data, demonstrating the model's robustness.

Both of the simpler models are special cases of the LD2 family of models: the LD1 model requires the limb-darkening parameter $d_\lambda = 0$ in both I and V , while the UB model sets $c_\lambda = d_\lambda = 0$ in both bands. This means that our LD1 and UB models, which correspond to points on the χ^2 hypersurface over restricted portions of the LD2 parameter space, also correspond to points on the full LD2 χ^2 hypersurface. The probability of obtaining a renormalized χ^2 that is larger than that of the LD1 solution is greater than 10% for both the DoPHOT and frame-quality methods of estimating relative photometric uncertainties; the probability of obtaining a renormalized χ^2 larger than that of the UB is negligibly small.

We conclude that the two-parameter limb-darkening model is clearly superior to the uniform source model and marginally superior to the one-parameter limb-darkening model. We now adopt it as our best model and use it to derive the physical parameters for the lens and the surface brightness profile of the source, which we now compare to expectations from stellar atmosphere models.

4.2. Comparison to Stellar Atmospheric Models

As we discussed in § 2, both spectroscopic and photometric considerations indicate that the source star of 97-BLG-28 is a K giant in the Galactic bulge, with K2 III being the most probable type. The fits to our photometric data discussed in § 3 yield the limb-darkening coefficients c_λ and d_λ for the V and I bands separately. The corresponding surface brightness profiles for the source star, normalized so as to give a total flux equal to unity, are shown in Figure 8 for our LD2 model of the high-quality photometric data set using DoPHOT estimates for the relative photometric

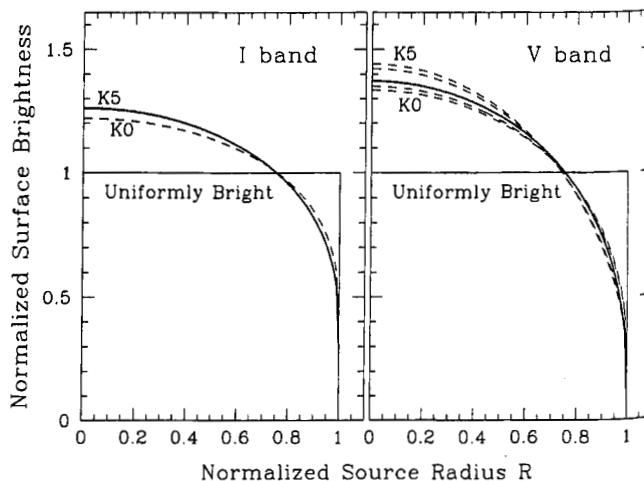
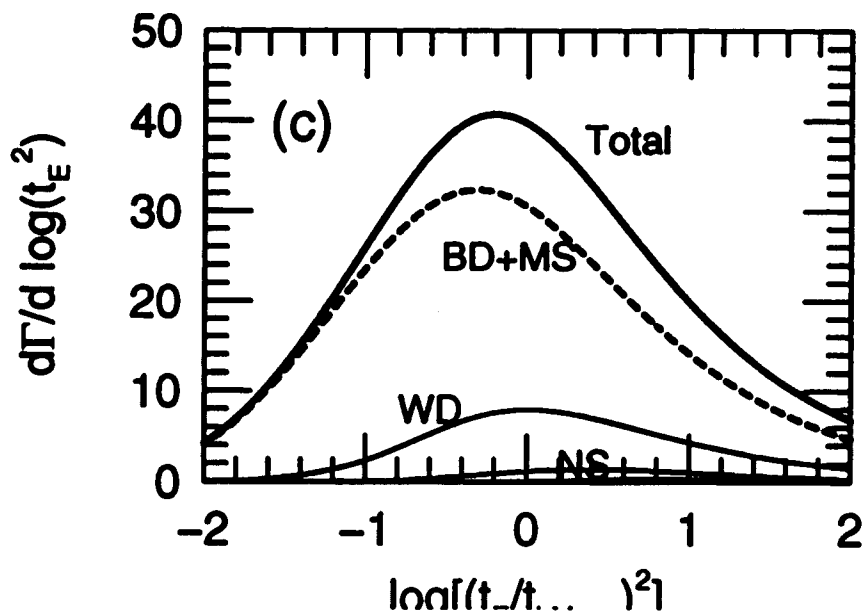
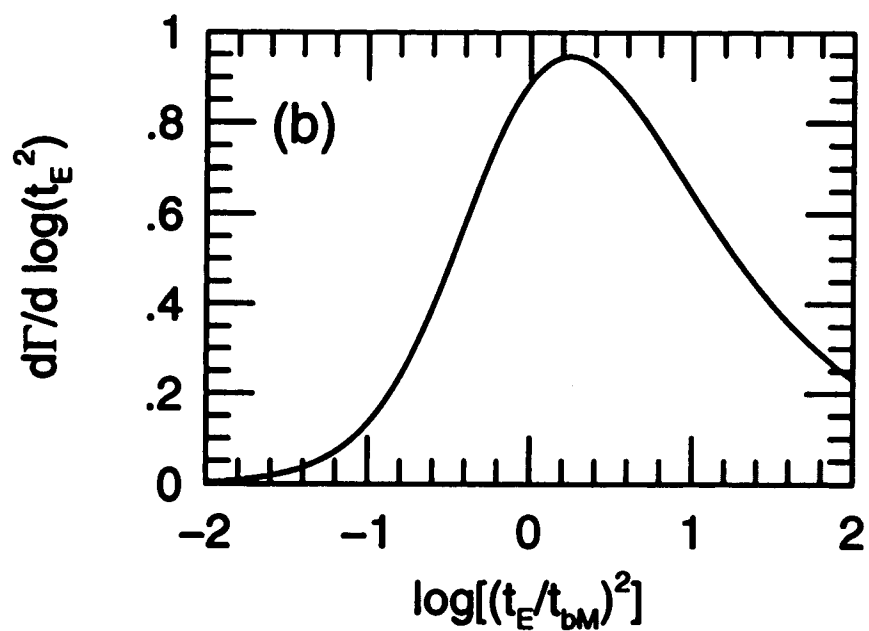
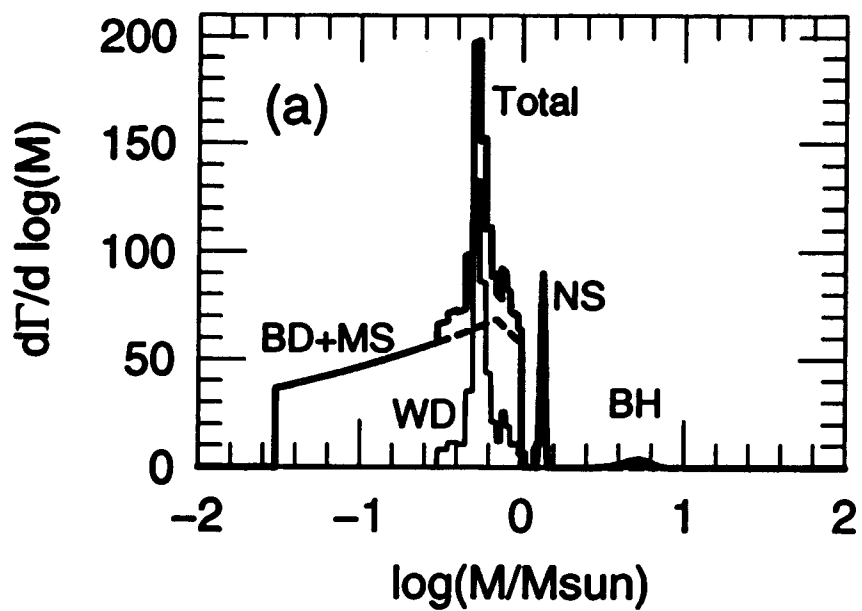


FIG. 8.—Source radial profiles in the I -band (left) and V -band (right) for uniformly bright (thin solid line) and our two-parameter limb-darkened source (thick solid line) models. Also shown are the theoretical expectations in the Cousins I and Johnson V -bands based on atmospheric models for K0–K5 giants (dashed lines) from two different literature sources (see text).

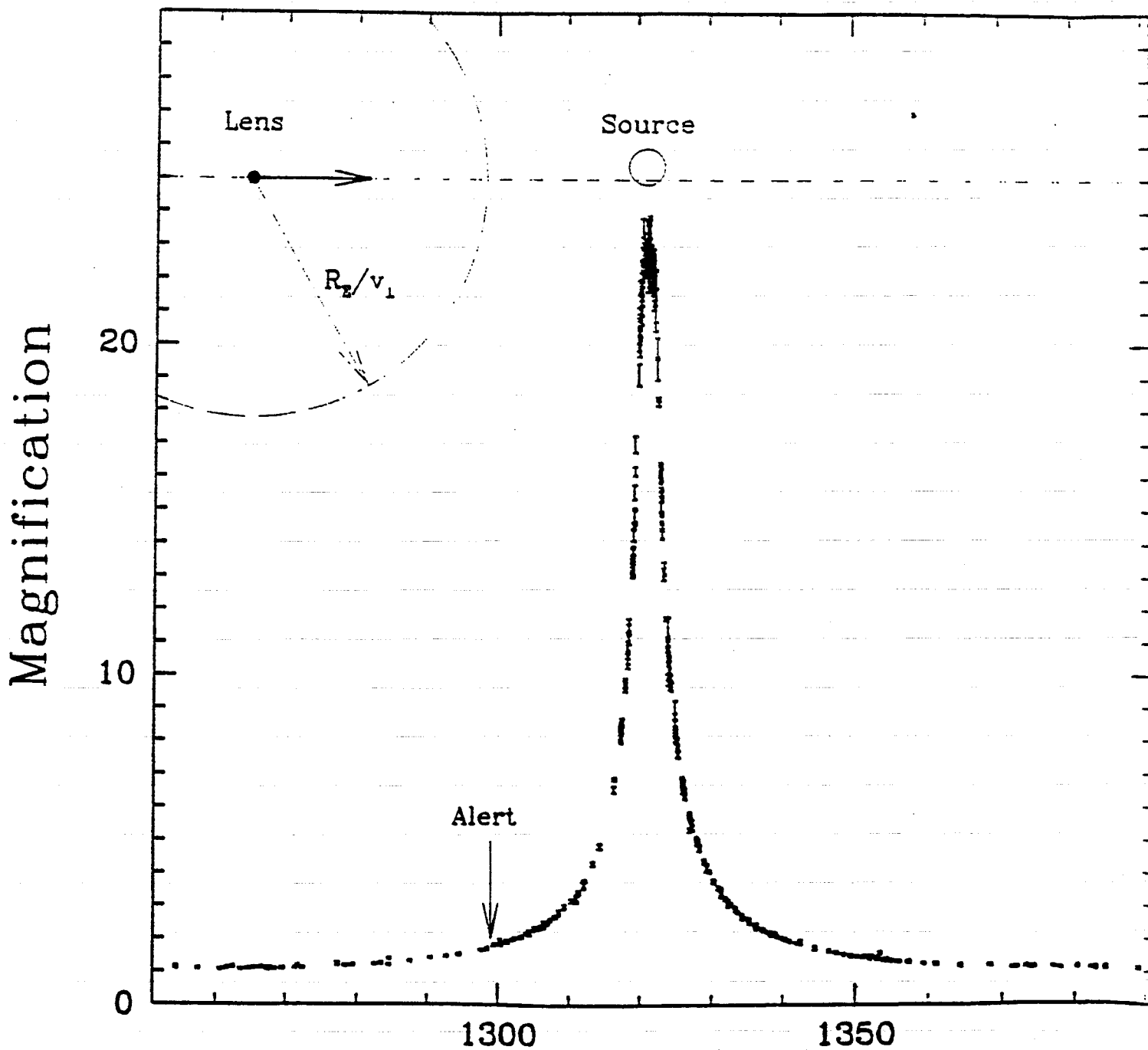


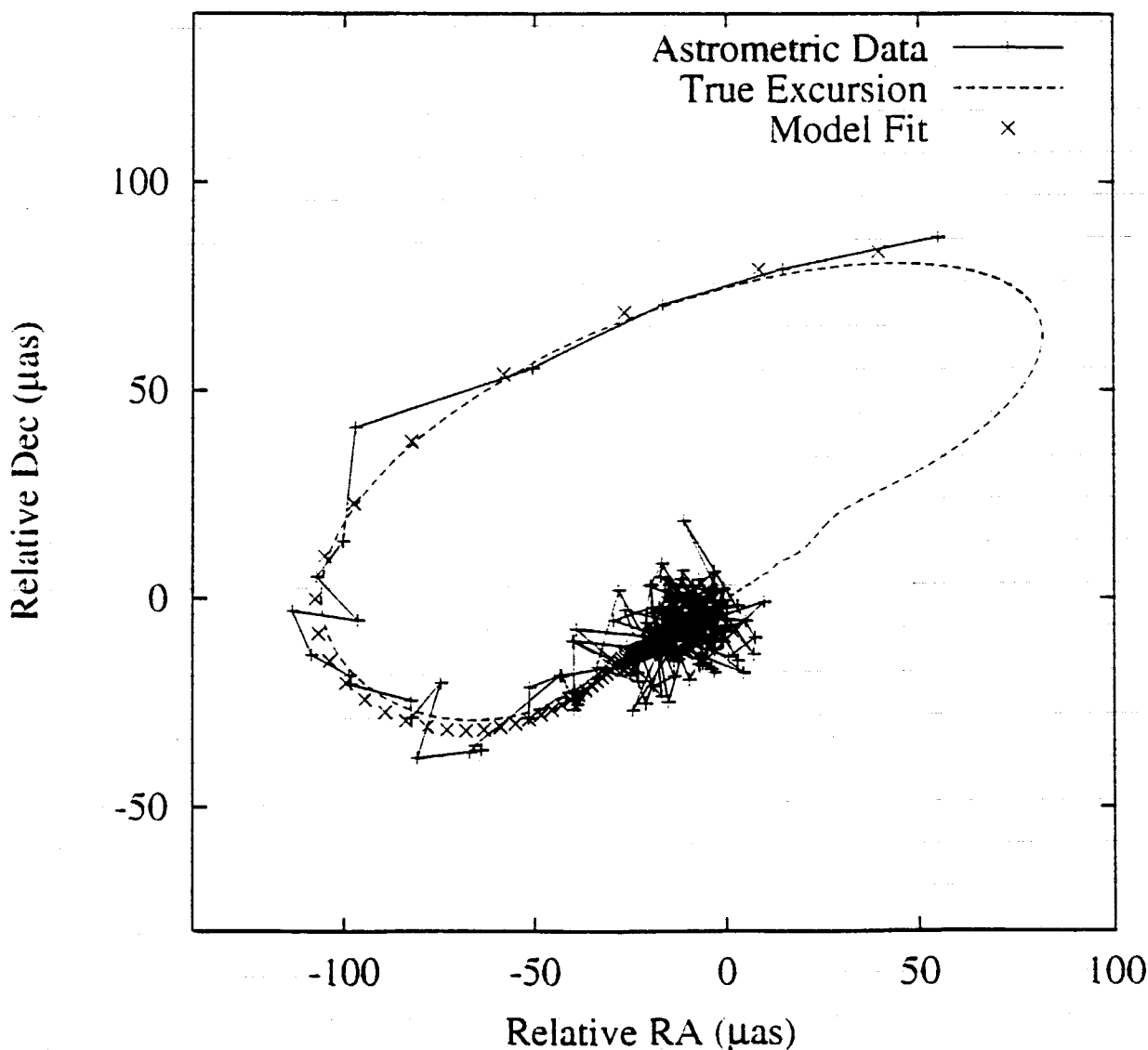
MACHO 95-30 ALERT

$$t_E = 34 \text{ days}$$

$$\theta_E = 430 \mu\text{as}$$

$$\mu_{\text{rel}} = 22 \text{ km/s/kpc}$$





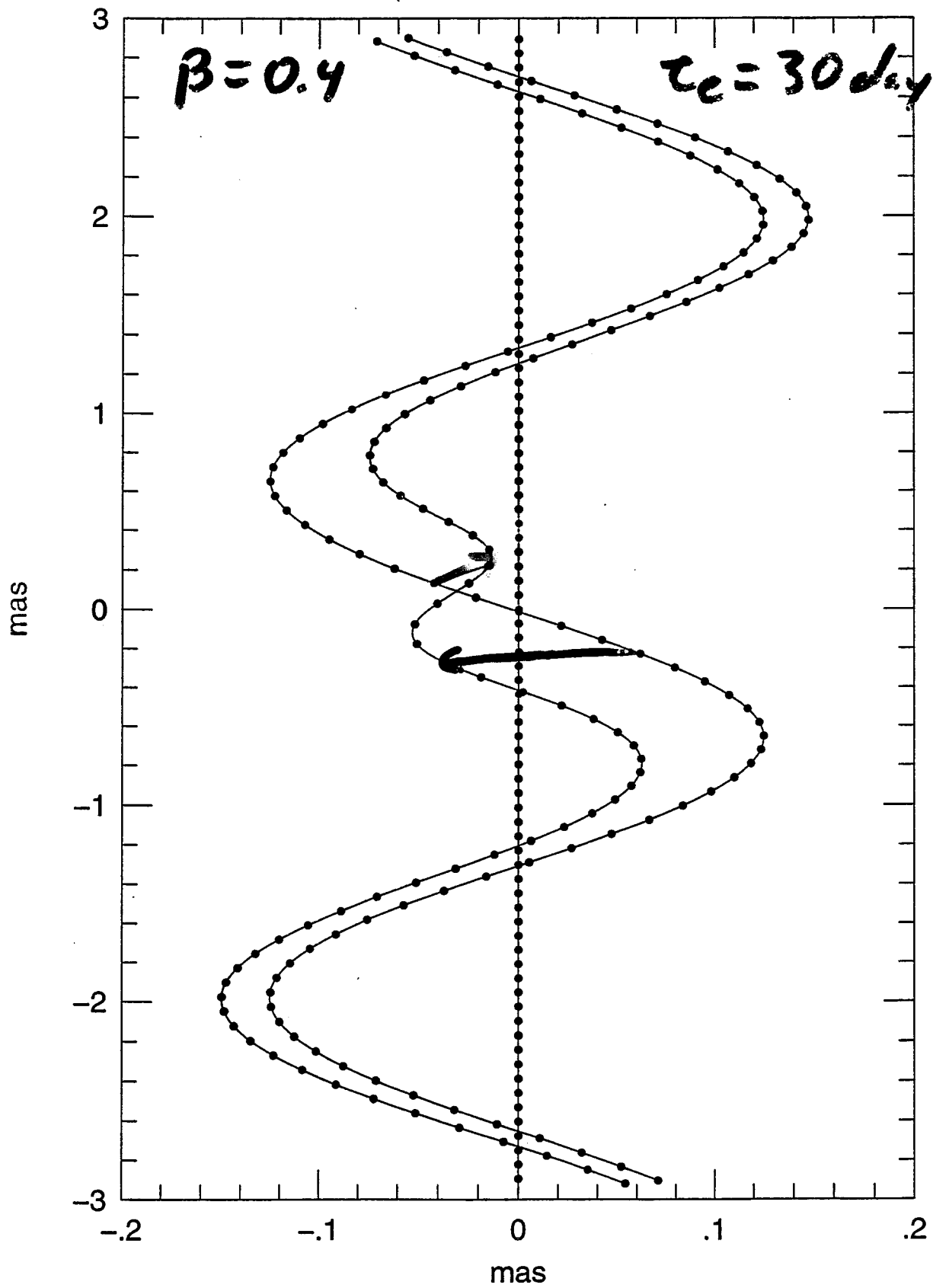
of fitting a microlensing model to synthetic terrestrial photometry and astrometry are a lens motion position angle of 30° , $p = 0.4$, $r_E = 300 \mu\text{as}$, and $\Pi = 100 \mu\text{as}$ that differential astrometric measurements commence after that detection. The astrometric and astrometric data. Shown in each are the simulated data, true values, we assume 3% rms error photometry. The time units on the x-axis are plotted

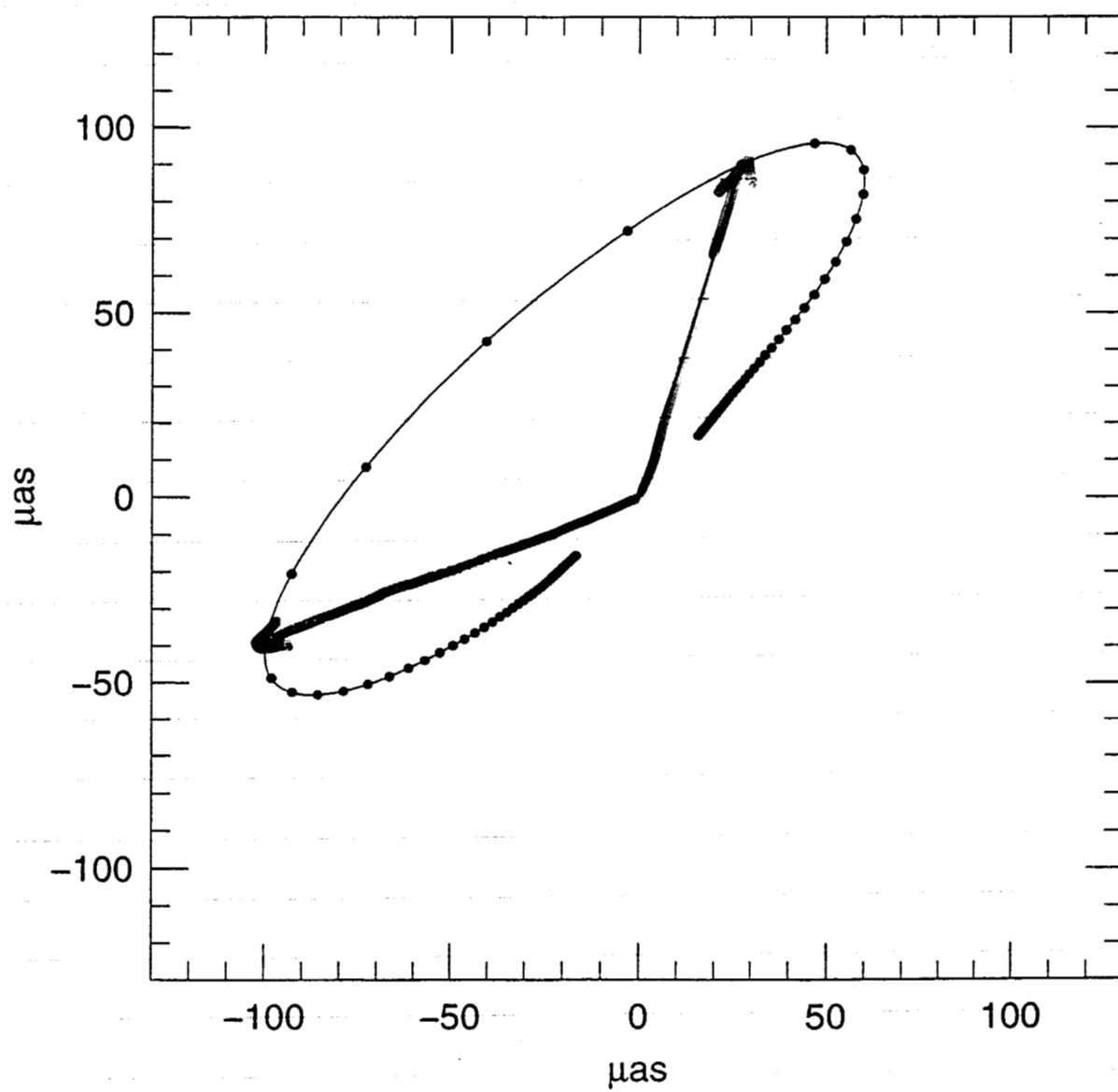
$$\theta_e = 310 \text{ mas}$$

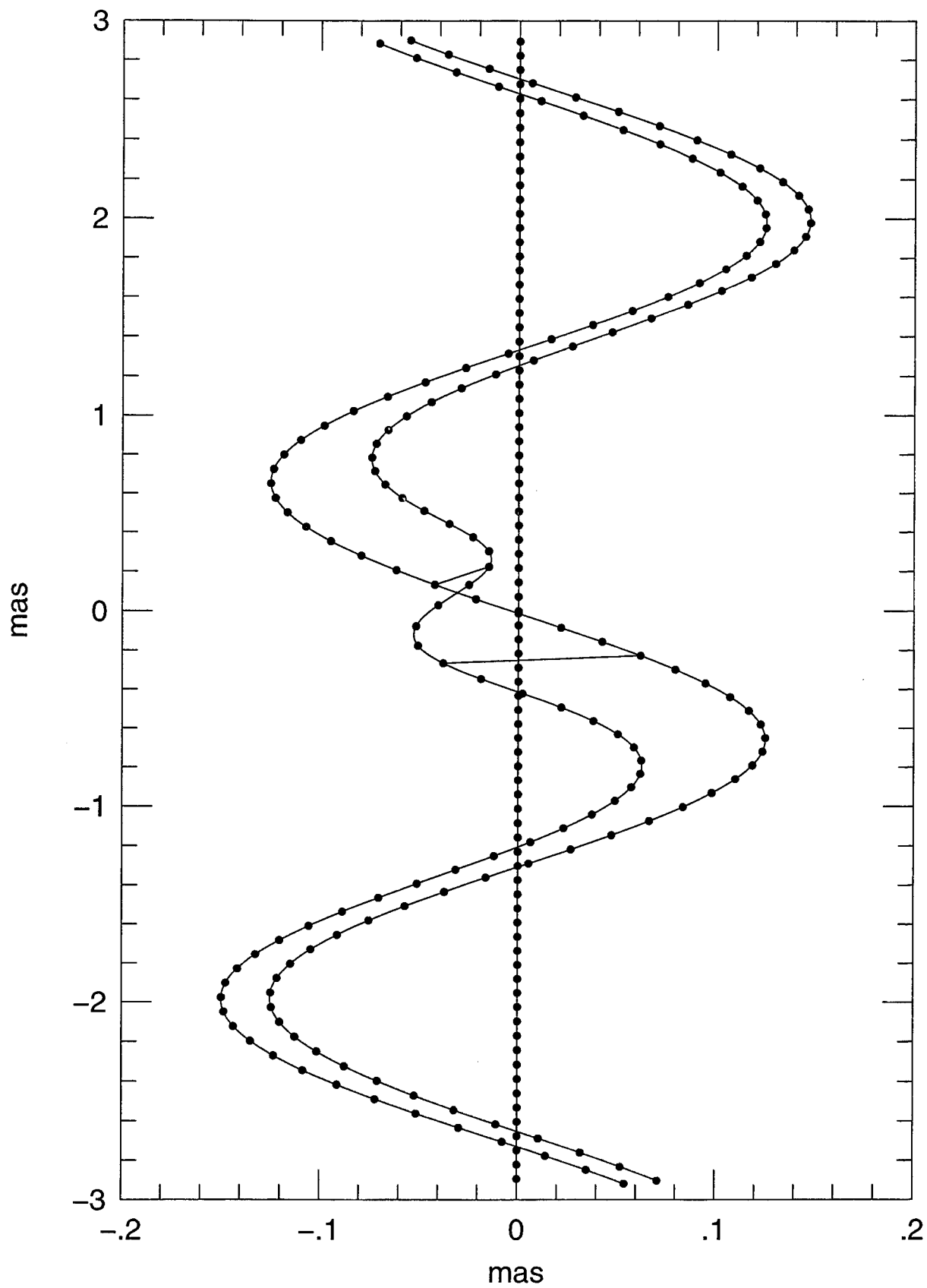
$$\pi_s = 125 \text{ mas}$$

$$\tilde{r}_e = 7.6 \text{ AU}$$

$$\mu_3 = 7 \text{ mas/day}$$







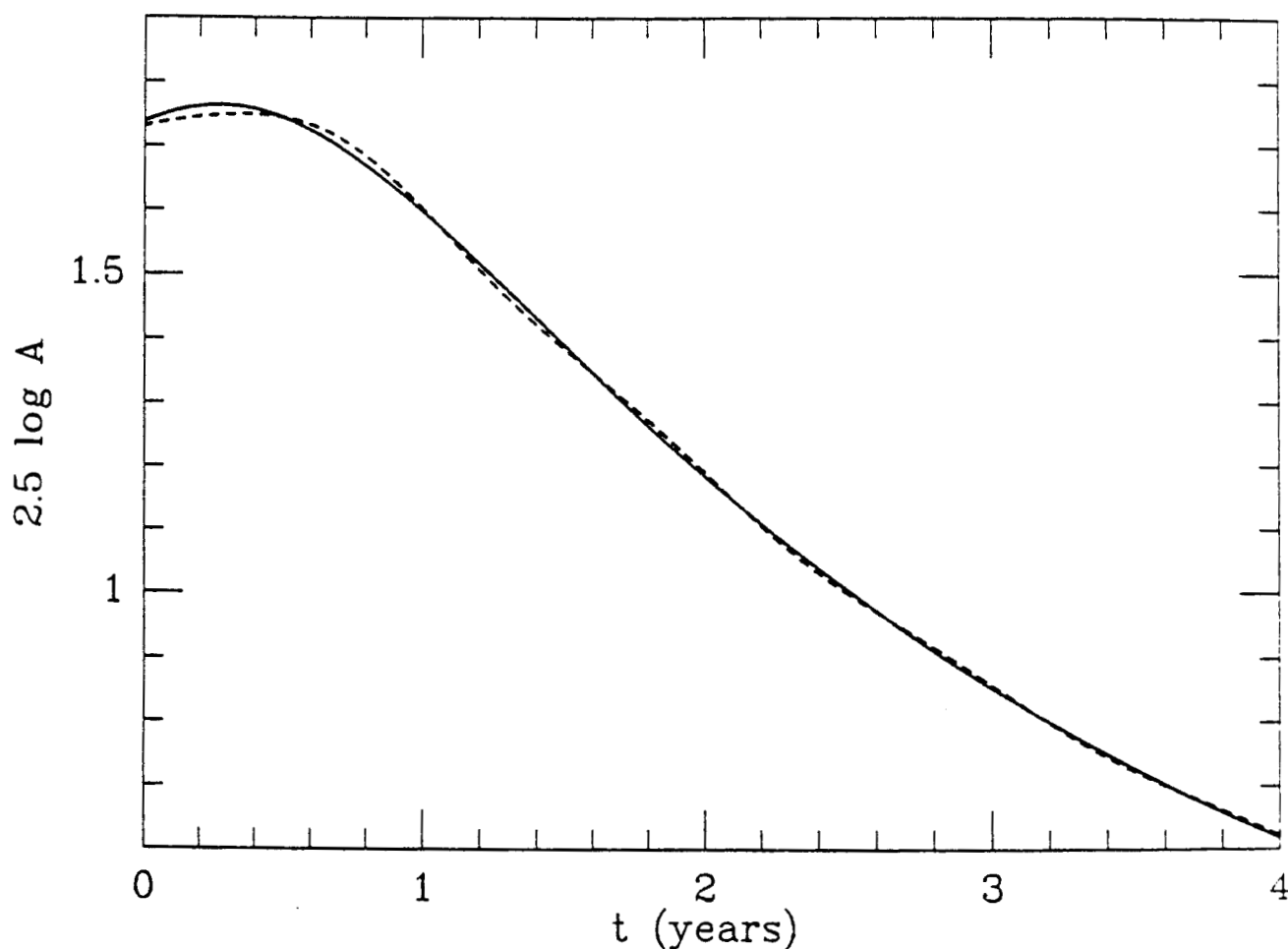


FIG. 2.—Magnification in magnitudes for a lensing event shown both with (*dashes*) and without (*solid*) correction for the Earth's motion. The lens is assumed to have mass $M \sim 10^3 M_{\odot}$, distance $D_{\text{OL}} \sim 10$ kpc, and transverse speed $v \sim 200 \text{ km s}^{-1}$. At maximum magnification, ($x_{\odot} = \beta = 0.2$) the phase of the Earth's orbit is offset by 20° relative to the projected lens-Sun vector. The Einstein ring is ~ 300 AU.

The light curve in Figure 2 looks suspiciously like a lensing event. Nevertheless, because the beginning of the “event”

THEORY

$$\pi_E = 0.003$$

$$t_E = 6 \text{ yrs}$$

No. 2, 1992

EXTENDING TH

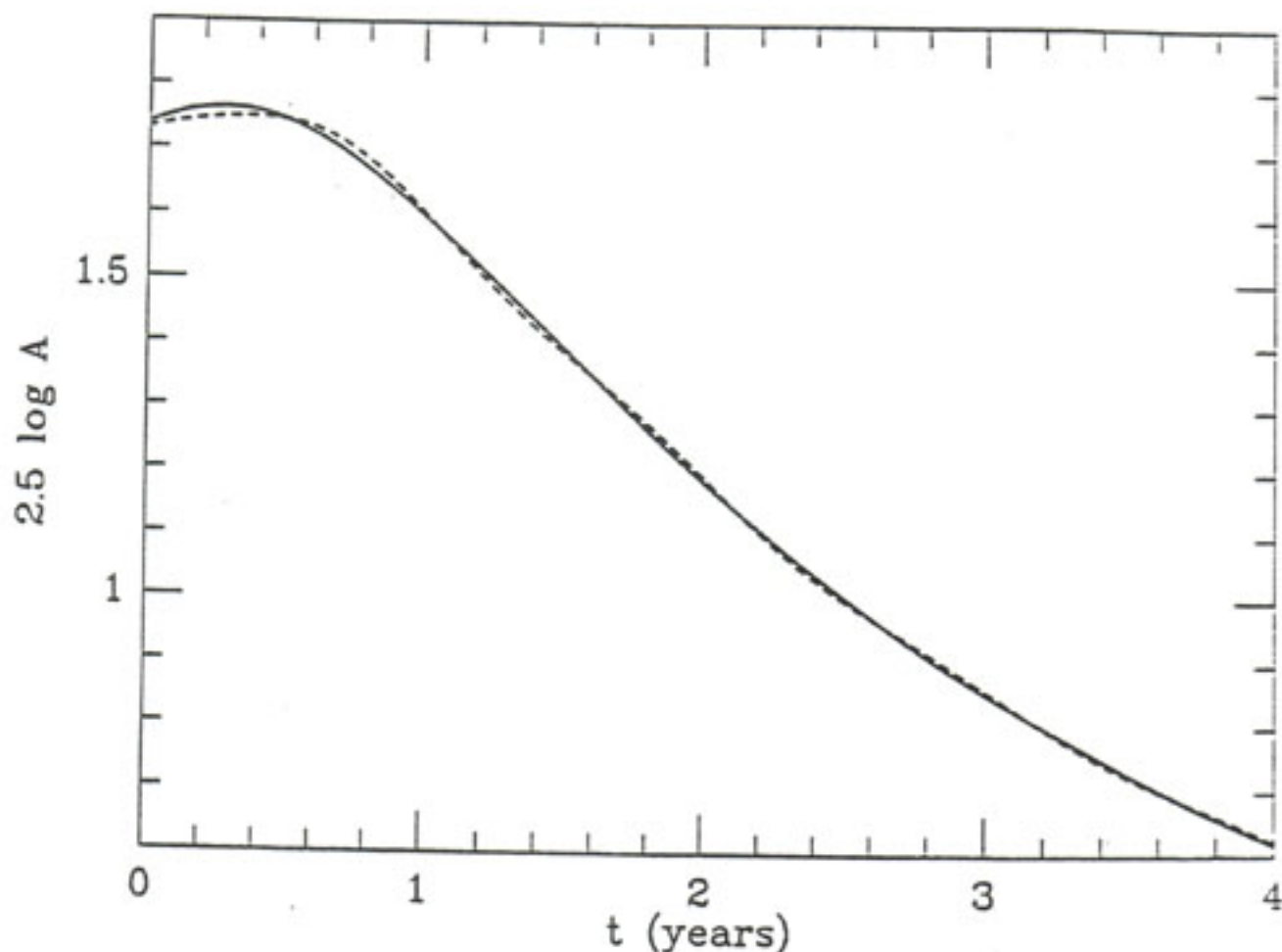
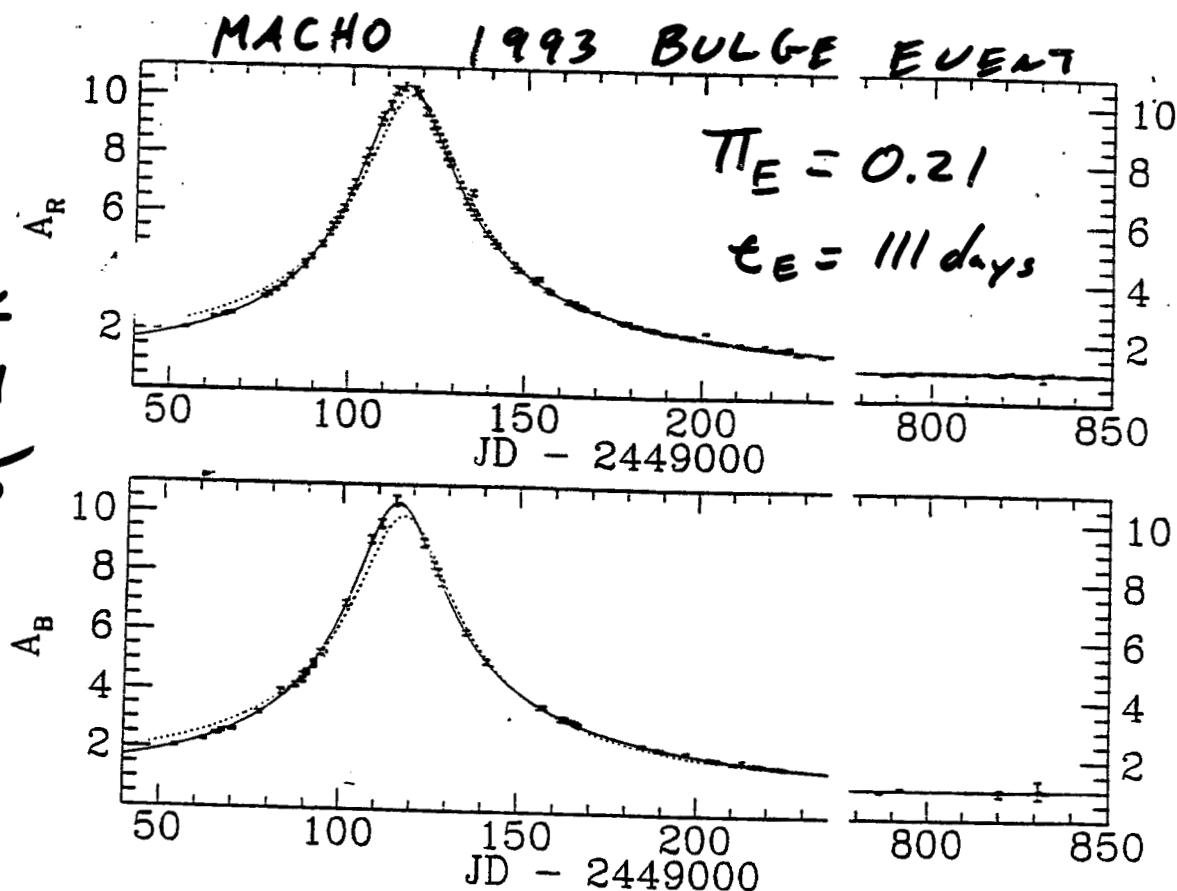


FIG. 2.—Magnification in magnitudes for a lensing event shown both with (dashes) and without (solid) correction for the Earth's motion. The lens is assumed to have mass $M \sim 10^3 M_\odot$, distance $D_{OL} \sim 10$ kpc, and transverse speed $v \sim 200 \text{ km s}^{-1}$. At maximum magnification, ($x_\odot = \beta = 0.2$) the phase of the Earth's orbit is offset by 20° relative to the projected lens-Sun vector. The Einstein ring is ~ 300 AU.

The light curve in Figure 2 looks suspiciously like a lensing event. Nevertheless, because the baseline is flat, it is not a lensing event.

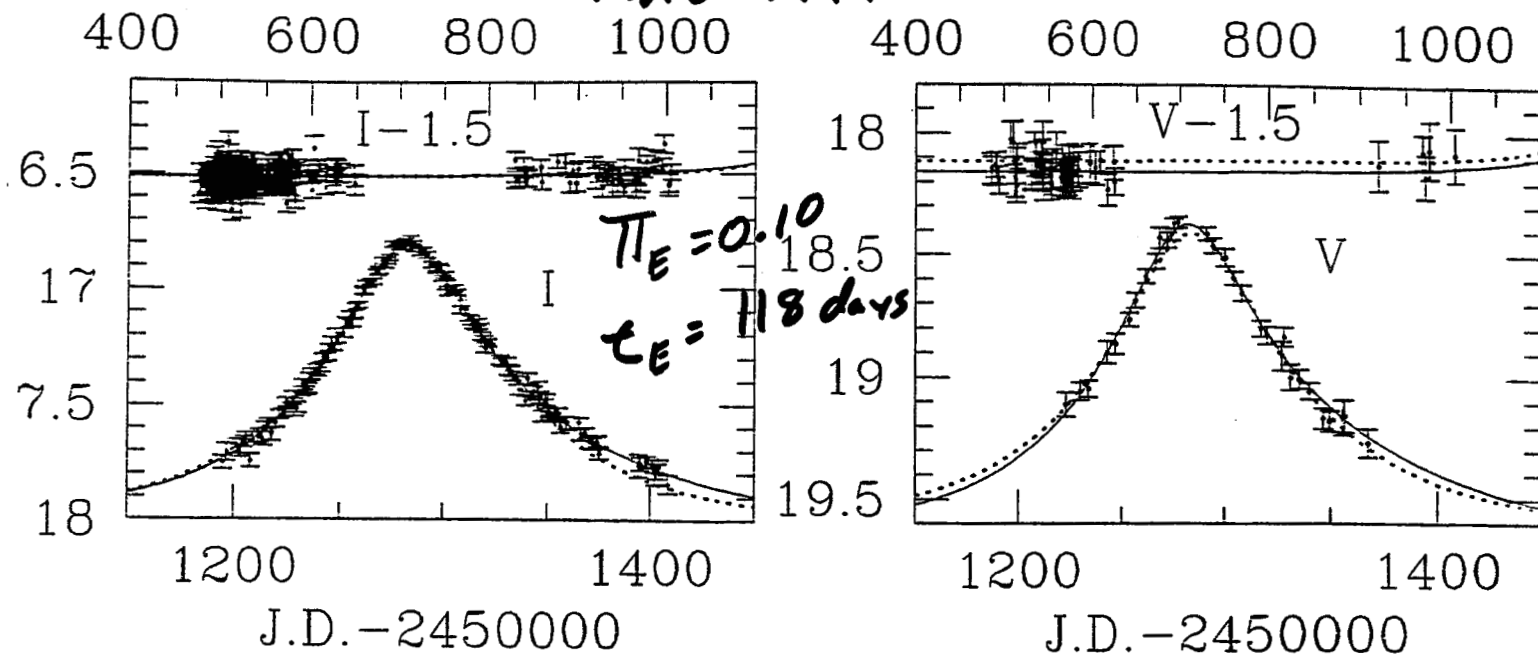
Alcock
et al
1995

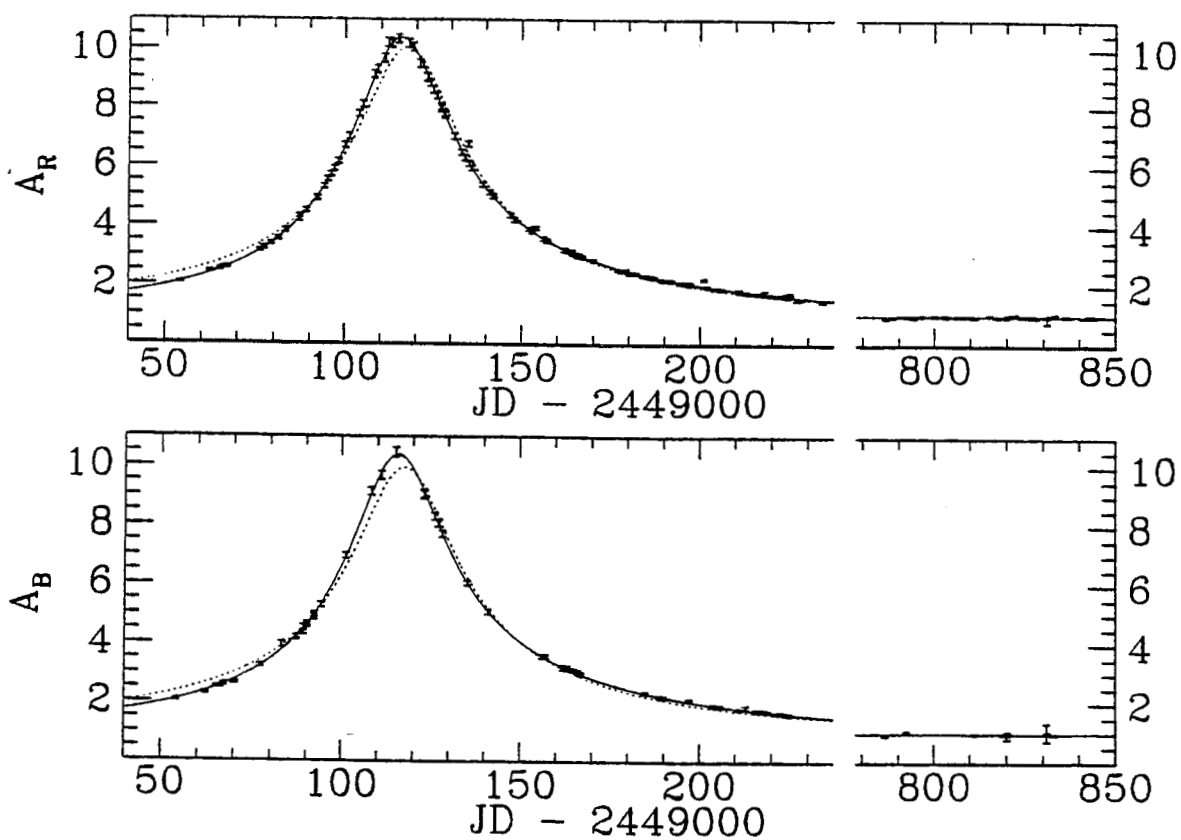


1999 OGLE CARINA EVENT

S. Mao: An ongoing OGLE parallax microlensing event toward Carina

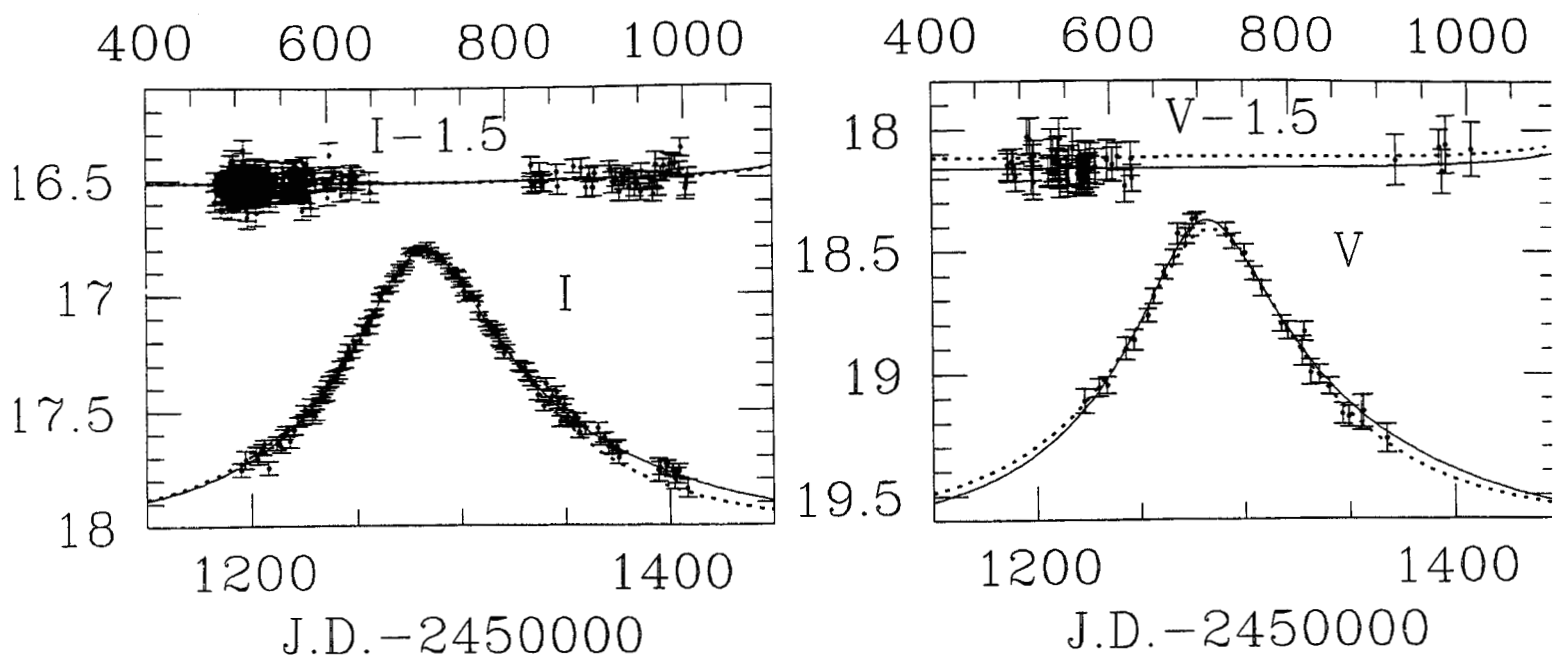
MAD 1999





L20

S. Mao: An ongoing OGLE parallax microlensing event toward Carina



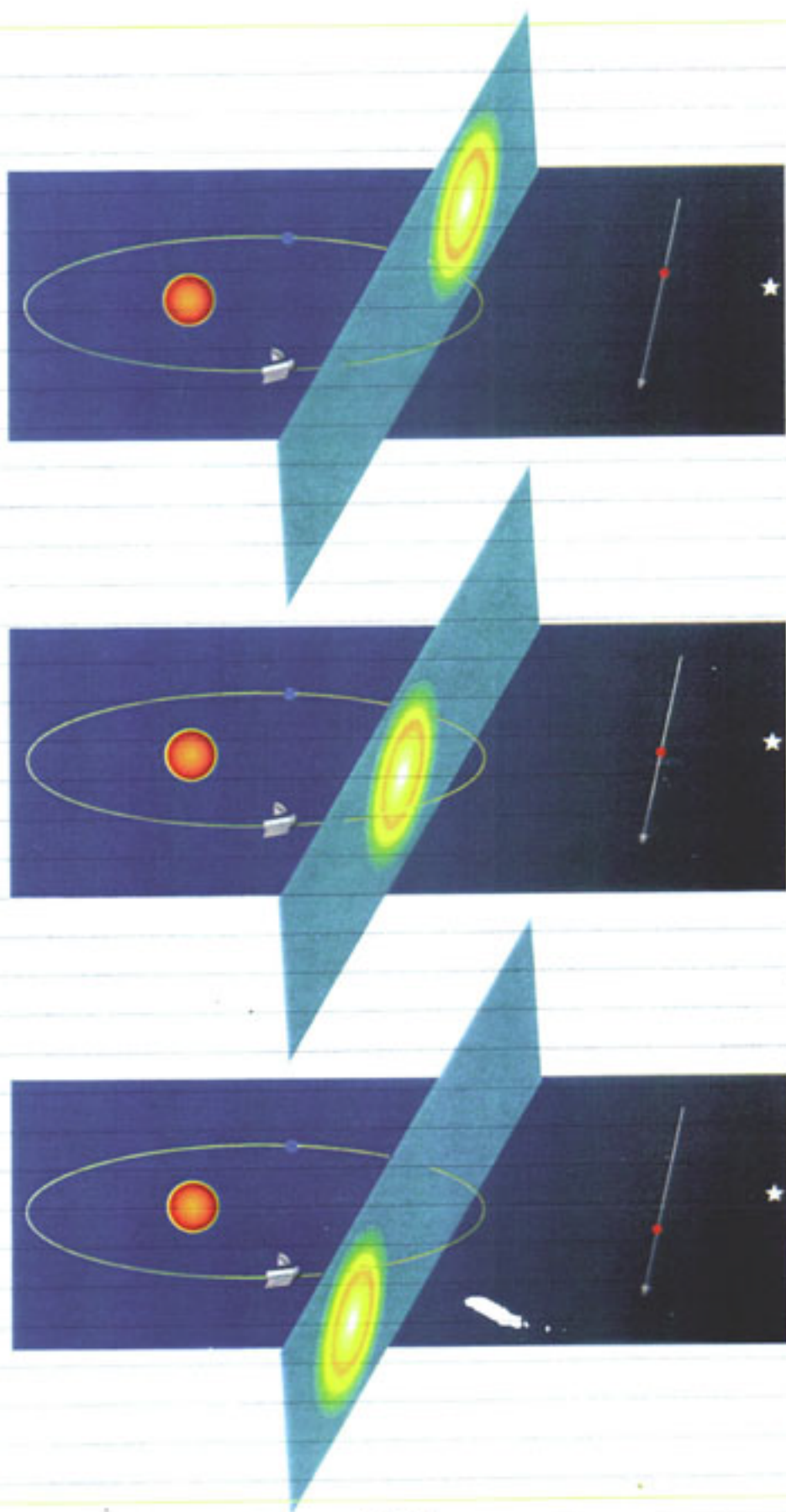
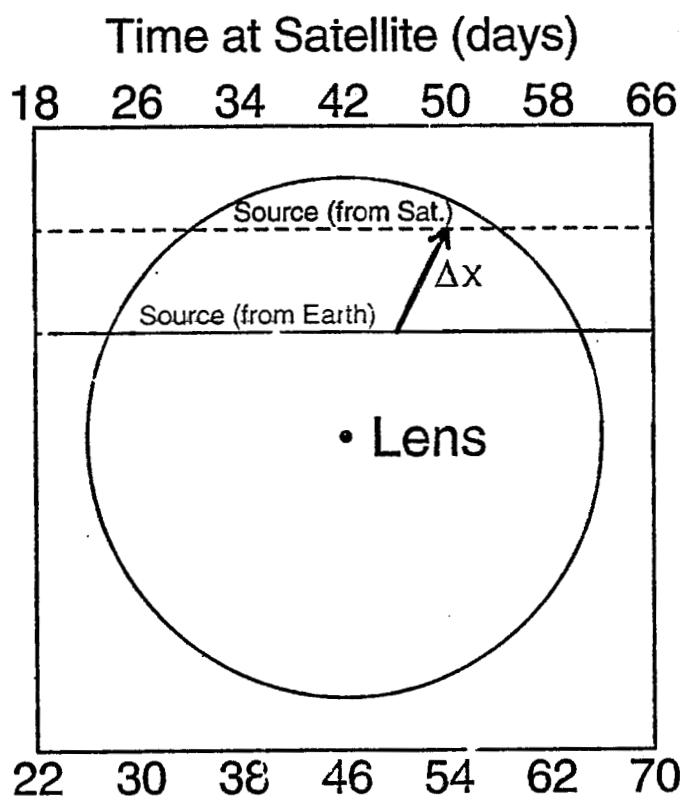
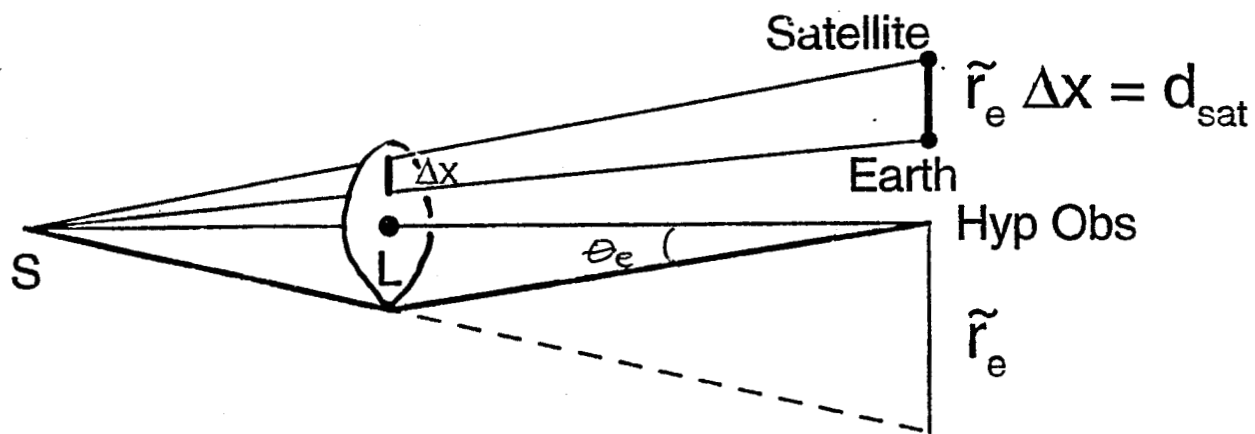
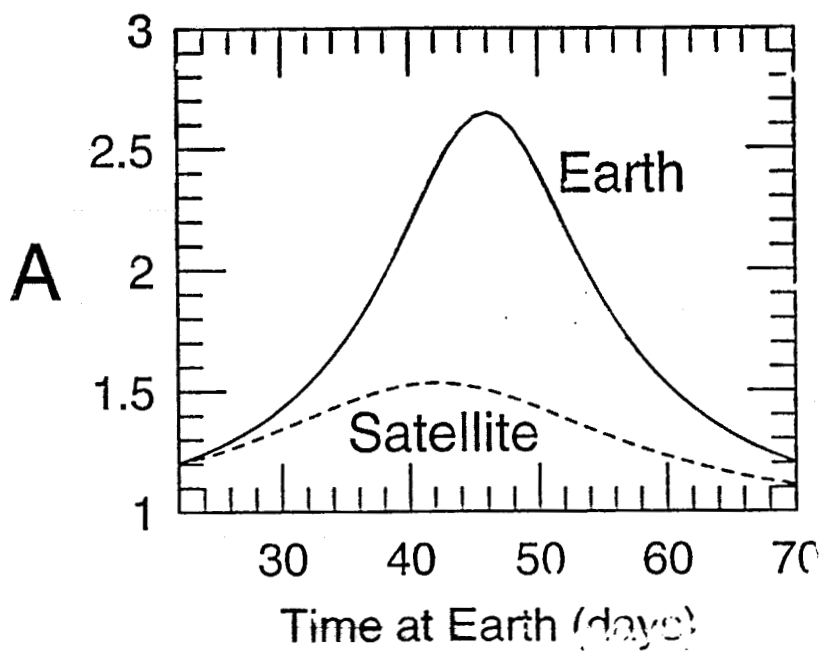


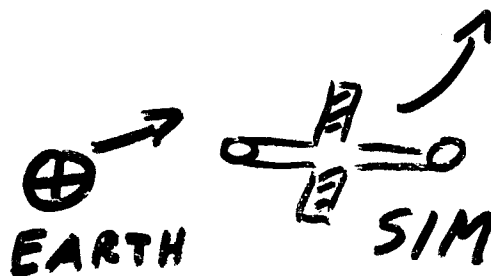
Plate 1



$$\tilde{r}_e = \frac{d_{\text{sat}}}{\Delta x}$$

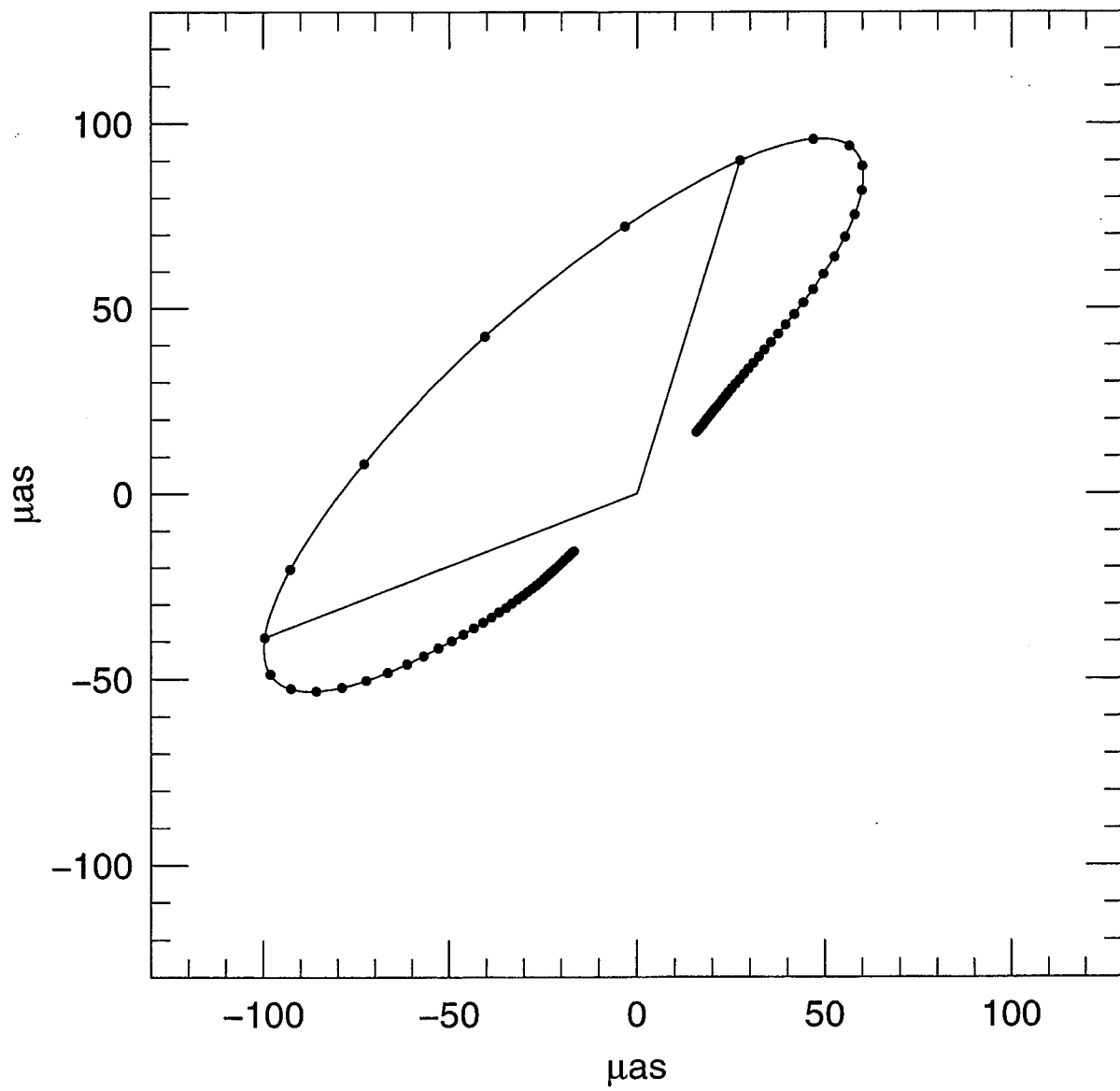


☺_{SUN}

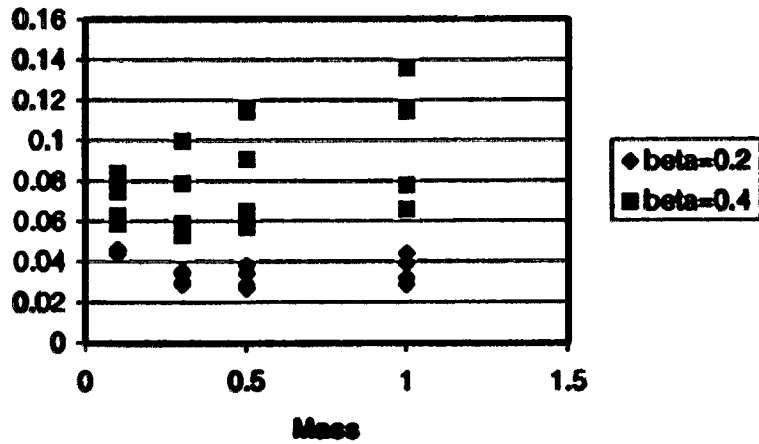


$$G_{\text{phot}} = \frac{G_{\oplus}}{t_3}$$

$$t_3 = \frac{\lambda}{\pi c} \sim 2.5 \text{ mas}$$



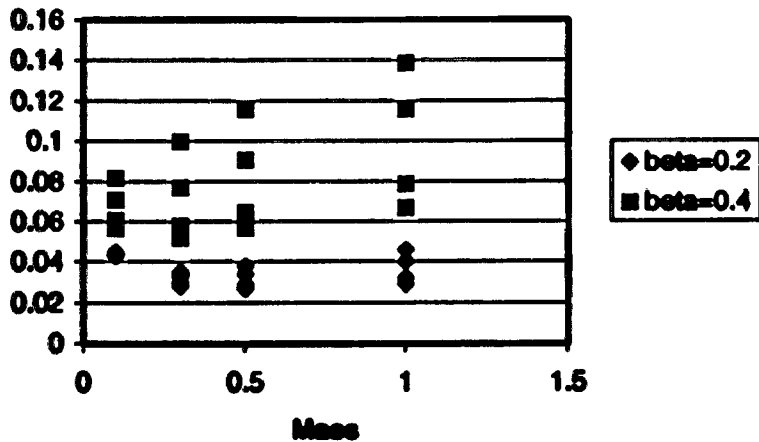
Mass fractional error BW



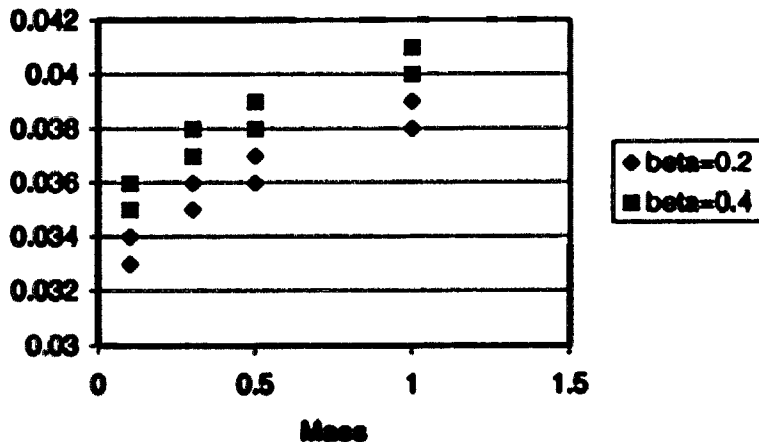
5 hours

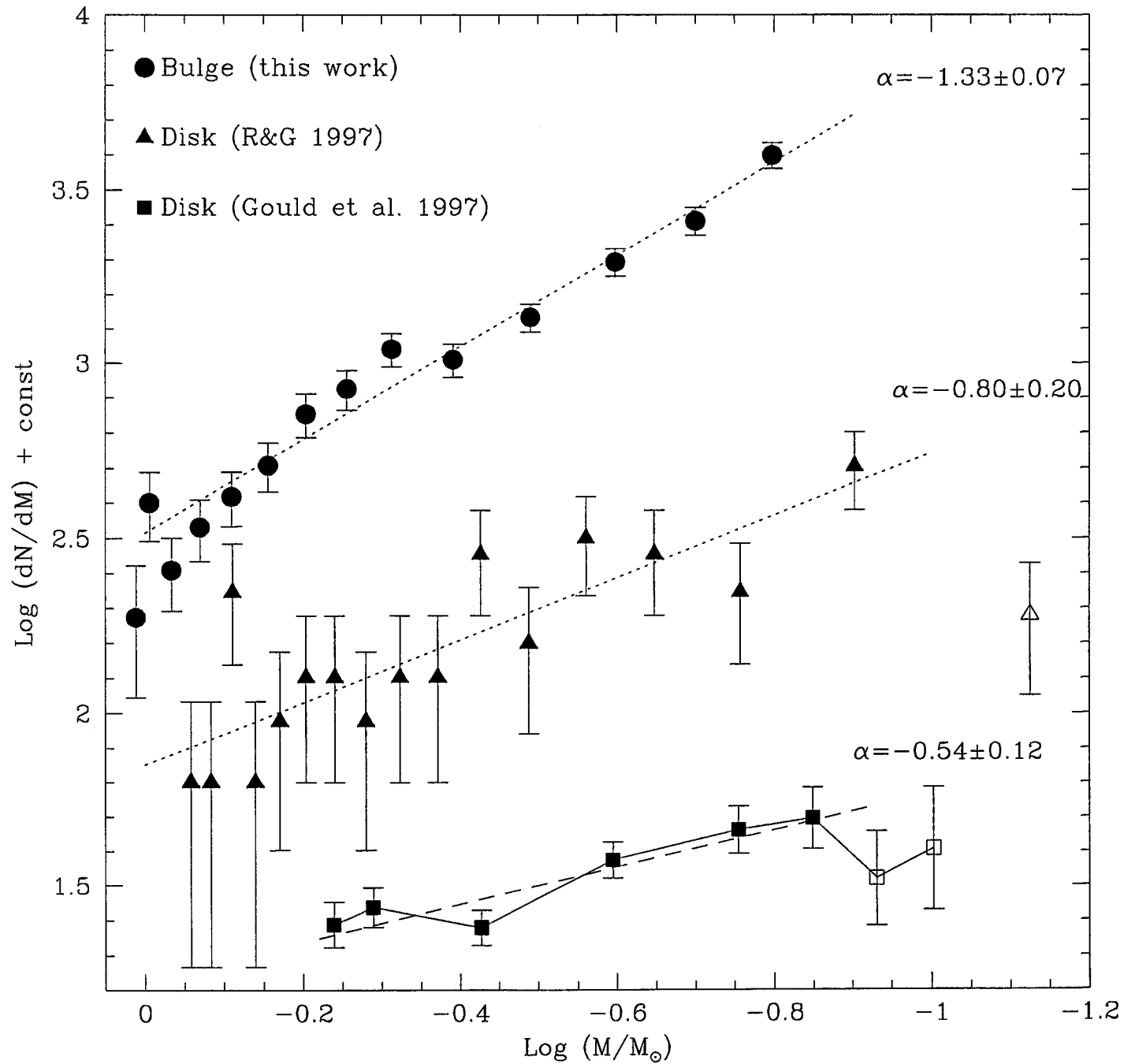
$I=15$

Distance fractional error BW

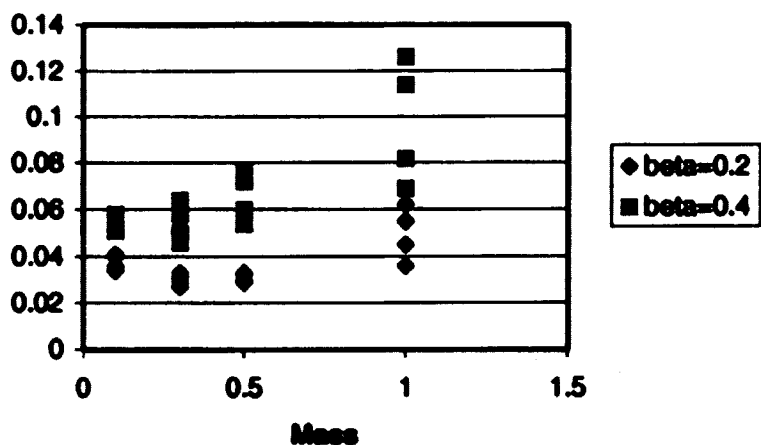


Parallax fractional error BW





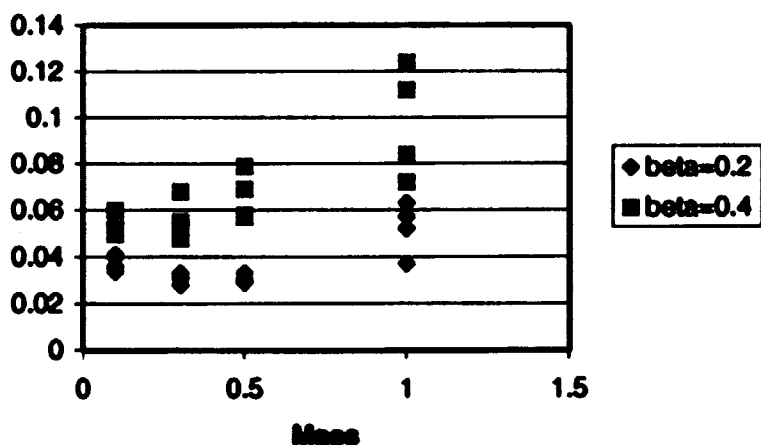
Mass fractional error LMC



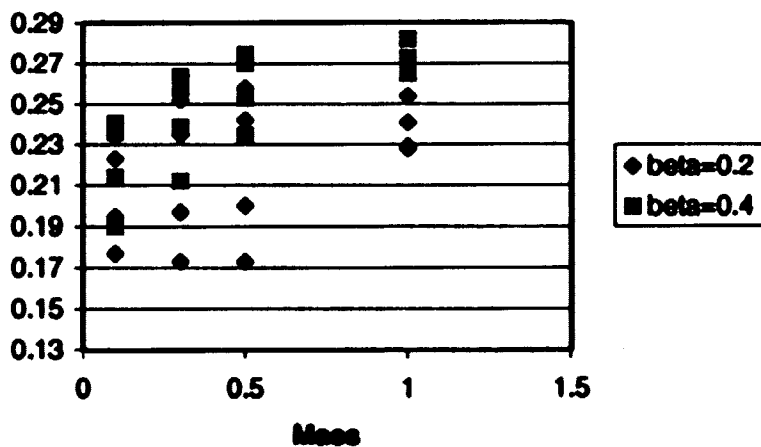
250 Hours

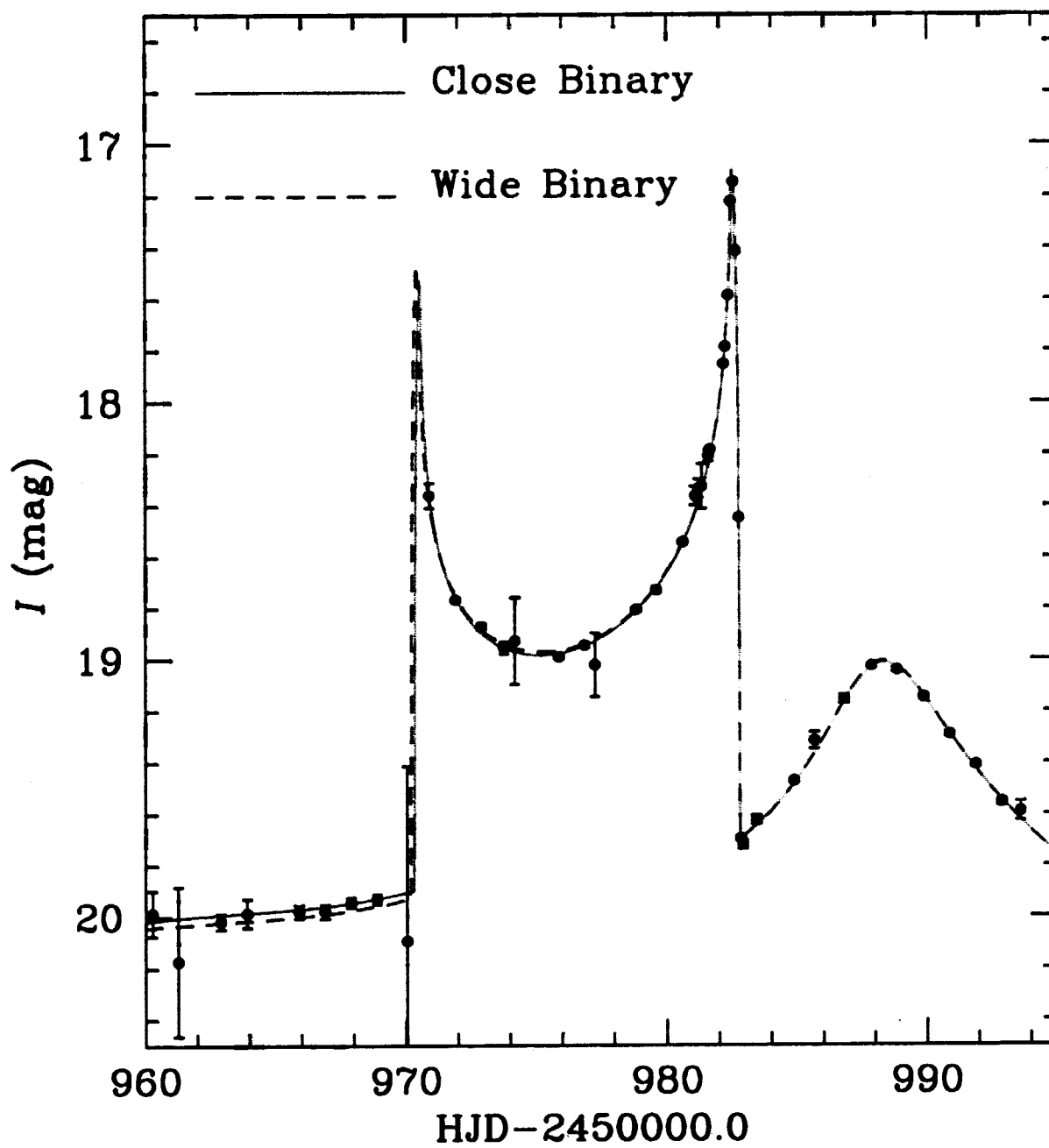
$V = 20$

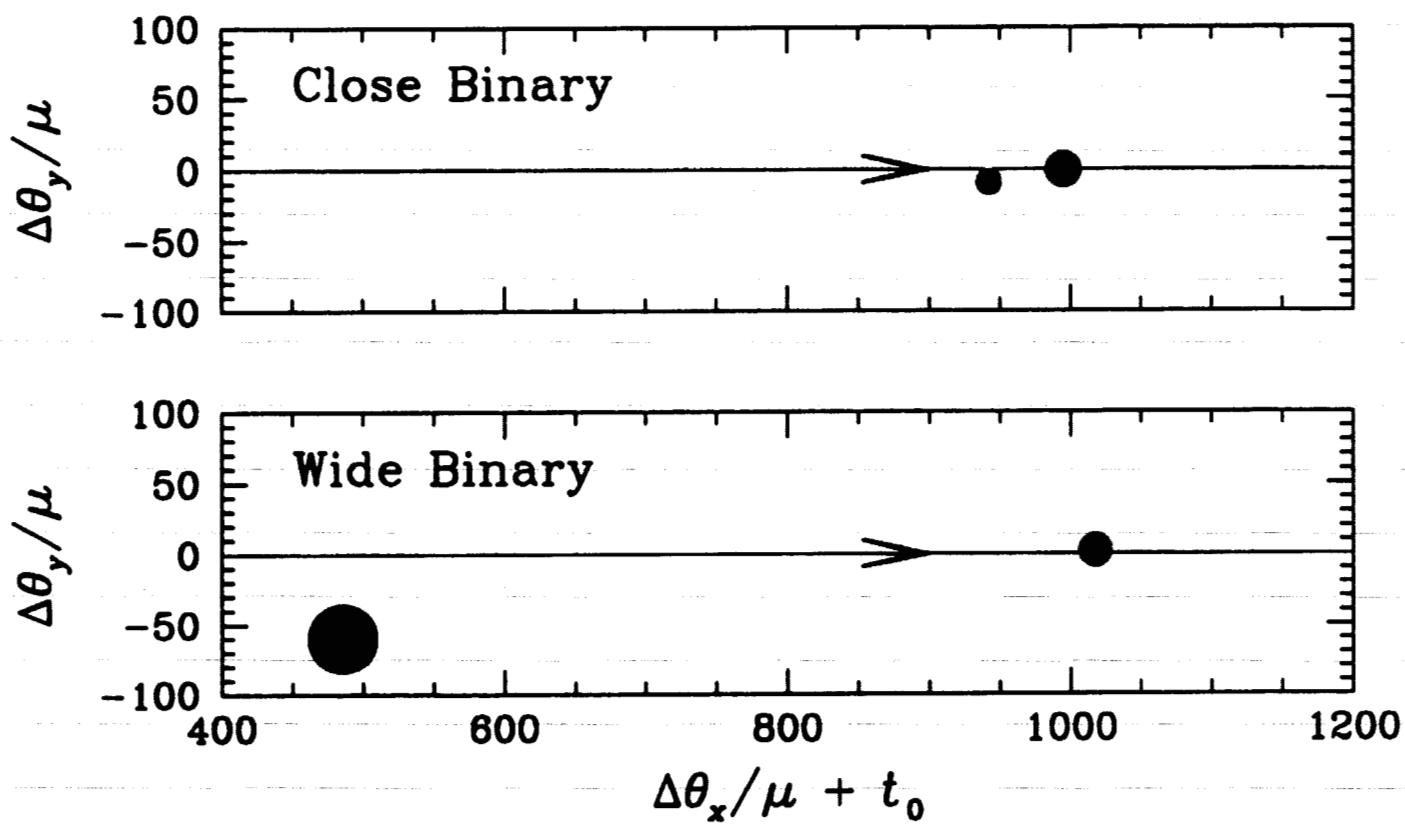
Distance fractional error LMC

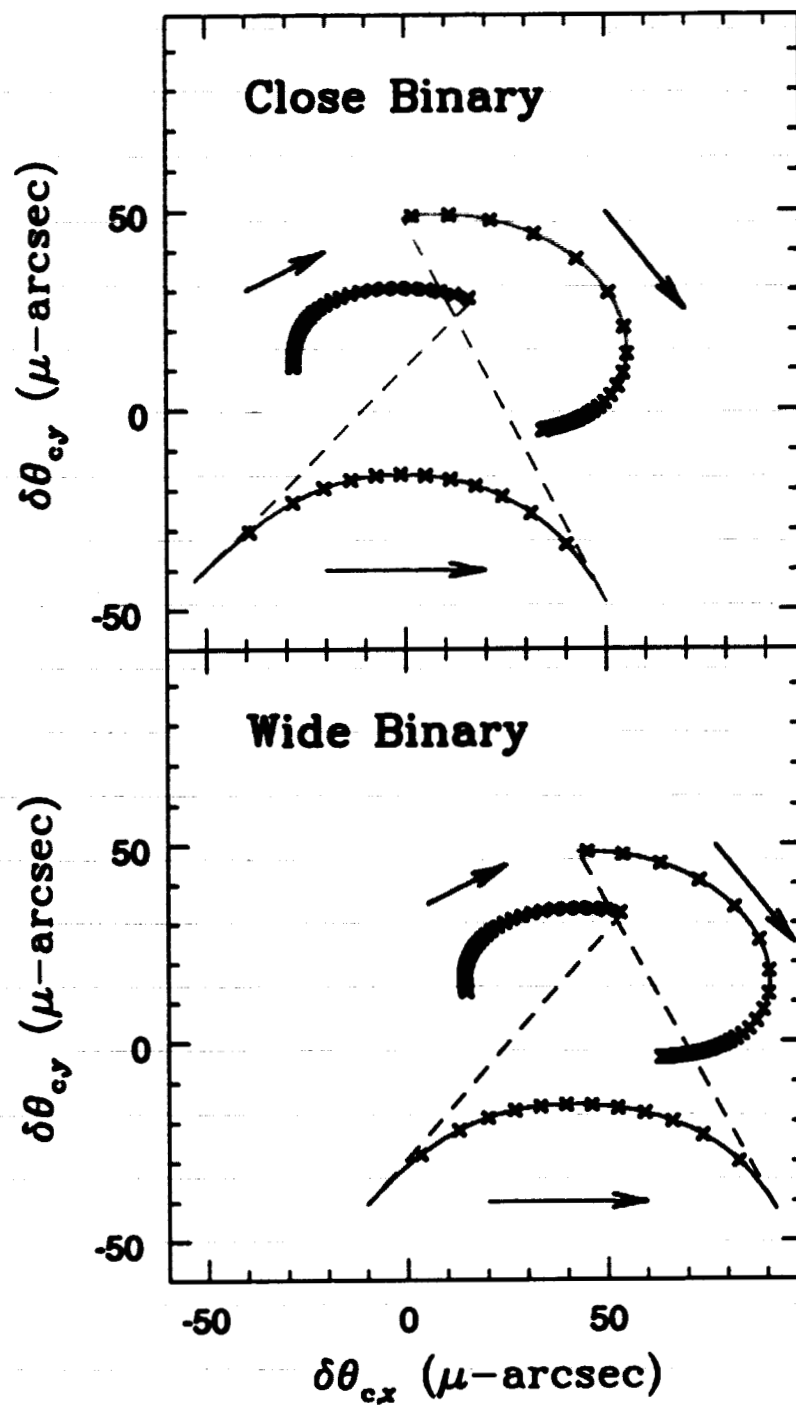


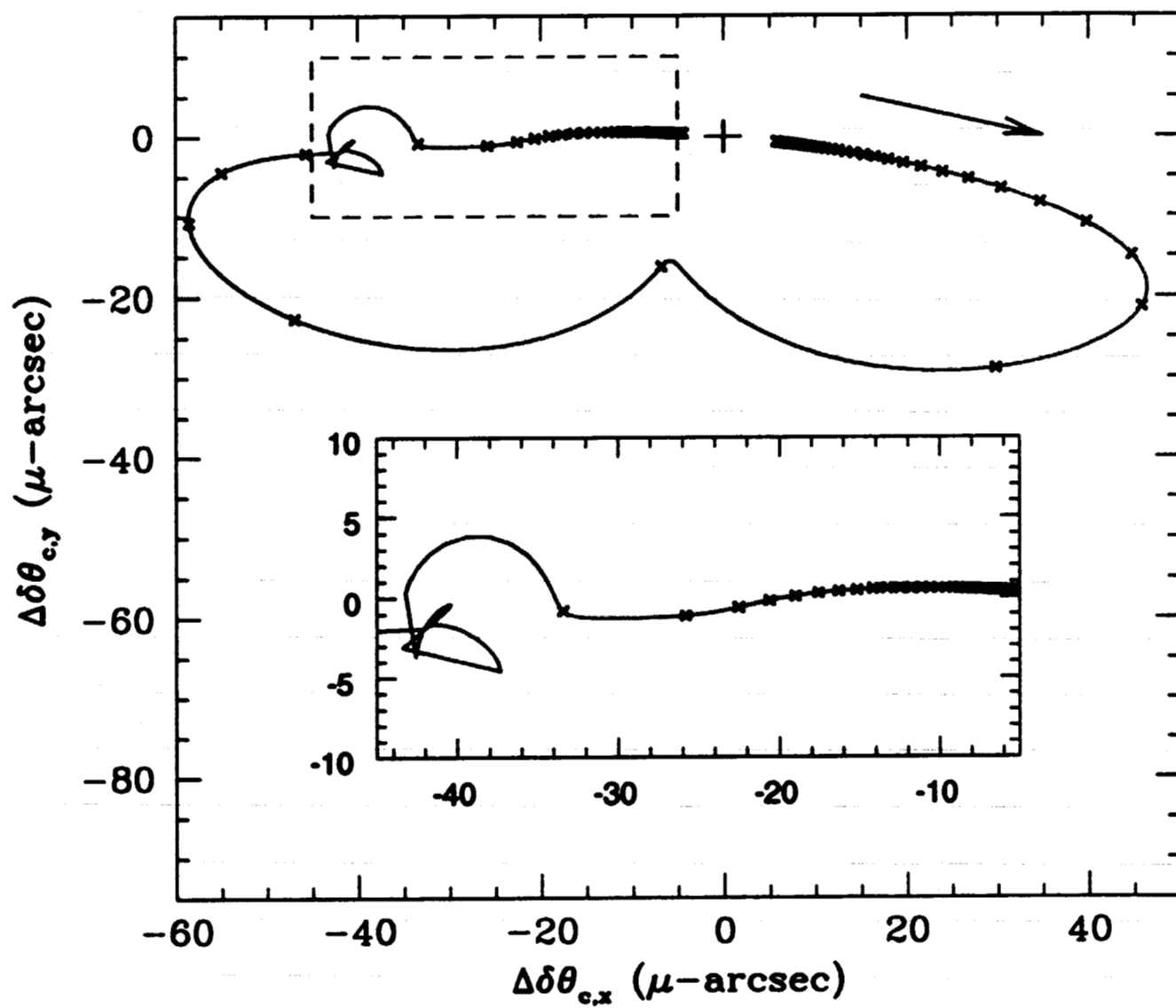
Parallax fractional error LMC











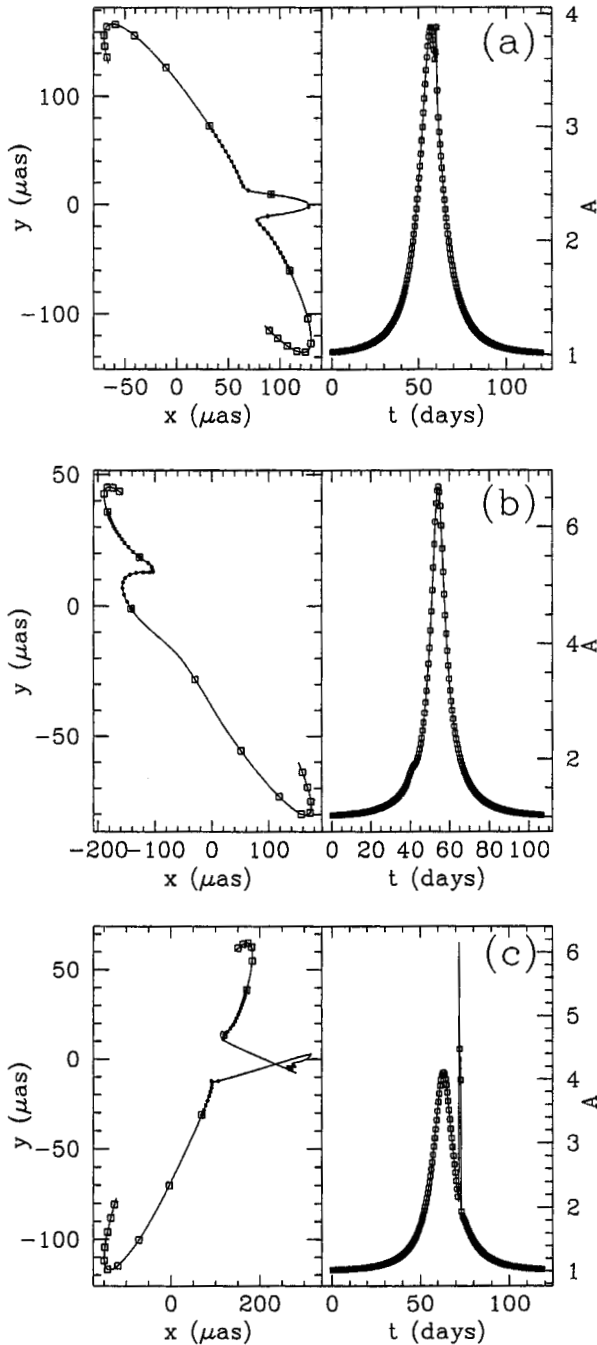


FIG. 2.—Some examples of planetary astrometric and photometric curves. All examples assume $q = 10^{-3}$, with a primary lens angular Einstein radius of $550 \mu\text{as}$, which corresponds to a Saturn-mass planet. Panel (a) has $u_p = 1.3$, panel (b) has $u_p = 0.7$, and panel (c) shows a caustic crossing event with $u_p = 1.3$. The time axis is scaled so that $\hat{t} = 40$ days, and squares are plotted one per week, so the durations of the deviations are of order 1 week. The dots are plotted every 12 hr during the deviation.

shorter length of time than in Figure 2c. Figure 3b shows a close-up of the effects that finite sources can have on the astrometric planetary signal. Depicted are the astrometric motion for stars of radius 1, 3, 5, 9, and $30 R_\odot$ traversing the same path in the source plane as in Figure 3a. As expected, increasing the source size smears out the signal, so that for $30 R_\odot$ the deviation is entirely washed out. Notice, however, that for 3 and $5 R_\odot$, the signal is easily visible, meaning that

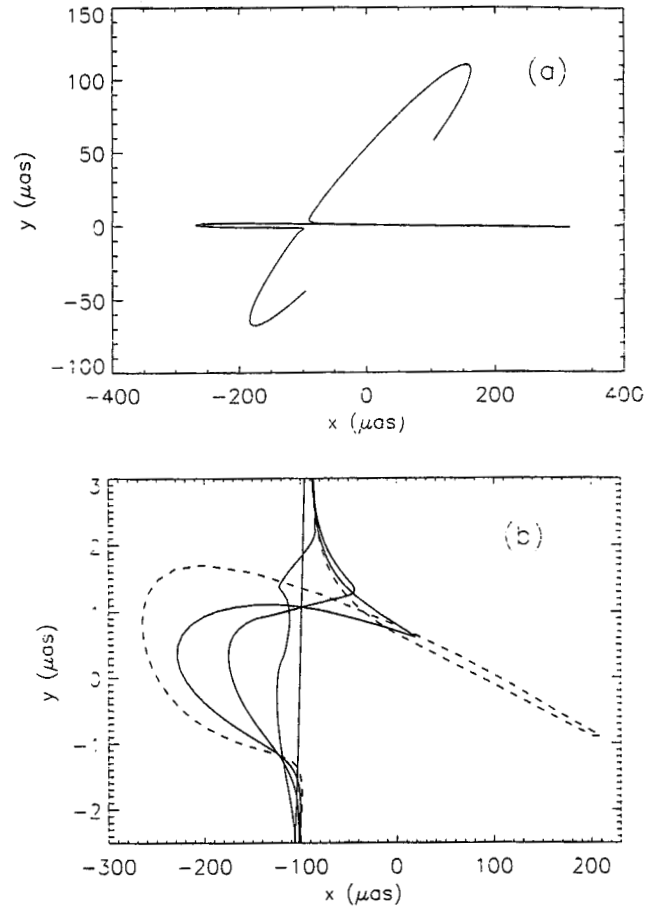


FIG. 3.—Astrometric motion for Earth-mass caustic crossing. Panel (a) shows the center-of-light motion for a point source, crossing a caustic associated with an Earth-mass planet at $u_p = 0.825$. The primary lens is $0.3 M_\odot$ at $D_l = 4$ kpc, and source at $D_s = 8$ kpc. Panel (b) shows a close-up view of the planetary deviation, with finite-size source. The dotted line plots the CoL motion for a $1 R_\odot$ size source. The solid lines depict the CoL motion for more realistic sizes typical of Galactic bulge stars, respectively 3, 5, 9, and $30 R_\odot$. Note the extreme anisotropy of the axes on the graph. For $\hat{t} = 40$ days the duration of the deviation is about 20 hr, with the center of the source spending roughly 90 minutes inside the caustic.

Earth-mass planets can in principle be detected using this technique.

4. PROBABILITY OF PLANET DETECTION USING ASTROMETRIC MICROLENSING

The possibility and probability of detecting planets with photometric microlensing have been explored by several authors (Mao & Paczyński 1991; Gould & Loeb 1992; Wambsganss 1997; Bennett & Rhie 1996; Peale 1997; Sackett 1997; Sahu 1997; Griest & Safizadeh 1998) and was found to be substantial. We wish to compare astrometric microlensing with these studies. In most of these studies, numerous light curves were generated for a range of planetary masses and projected orbital radii, and some simple detection criterion was established. In a realistic experiment, fitting of the planetary light curve would need to be performed and the planet mass determined before a planet detection was established. Parameter extraction with astrometry will be discussed below, but in the following section we will just use simple detection criteria analogous to those used in previous studies. We define as a detectable

MASSSES OF NEARBY STARS



$$\alpha = \frac{4GM}{c^2} \left(\frac{1}{d_L} - \frac{1}{d_s} \right)$$

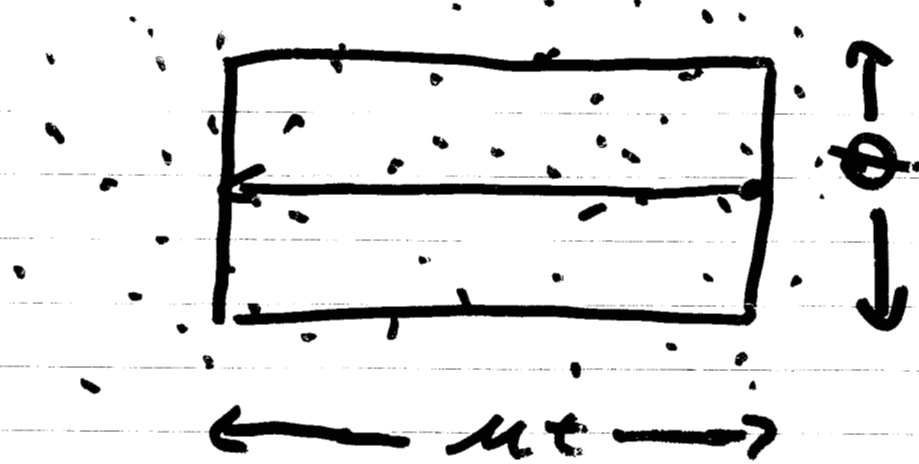
$$= 8 \text{ mas} \left(\frac{M}{M_\odot} \right) \left(\frac{\pi \text{ rad}}{1''} \right)$$

Refsdal 1964

Paczynski 1995, 1998

Miralda-Escude 1996

Individual Stars

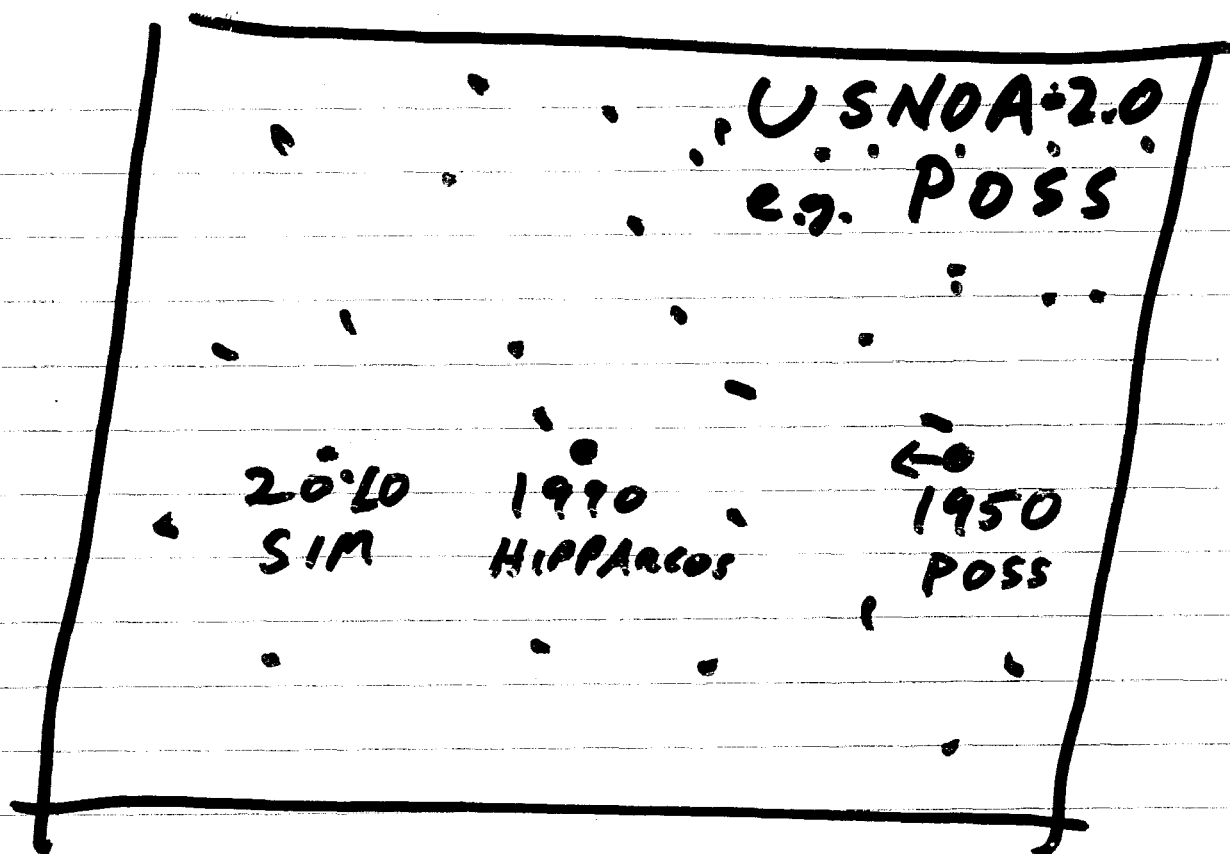


$$\phi \sim \frac{M}{d^2} \sim M\pi$$

$$\text{Prob} \sim N_{\text{BACK}} M\pi ut$$

Population

$$N_{\text{BACK}} \rho_{\text{ENS}} \pi_{\text{ENS}} u_{\text{ENS}}$$



HIPPARCOS 120,000

ACT 1,000,000

Luyten 50,000

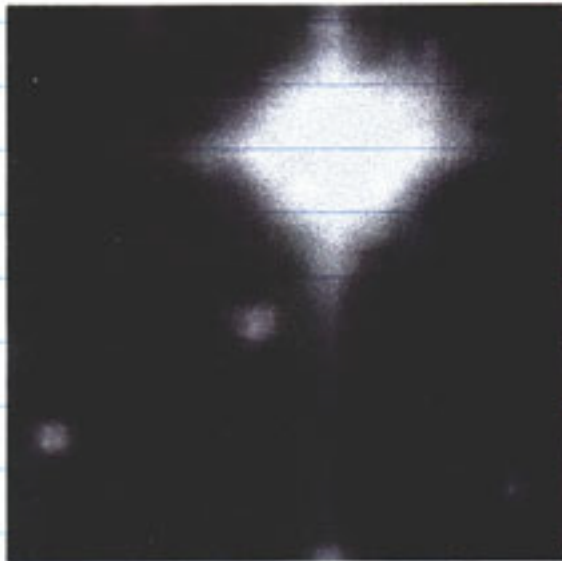
HD 250047

$V = 9.5$

$d = 46 \text{ pc}$

$\mu = 0.3''/\text{yr}$

1951
DSS 1



$1' \times 1'$

Source:

$V = 16.9$

1989
DSS 2



$1' \times 1'$

2012

$\tau_{\text{sim}} \approx 7 \text{ hr}$

$\beta = 0.5''$

61 Cyg A/B

$$d = 3.5 \text{ pc}$$

$$V_A = 5.2$$

$$V_B = 6.2$$

$$\mu = 5.2^{\text{mas}}/\text{yr}$$

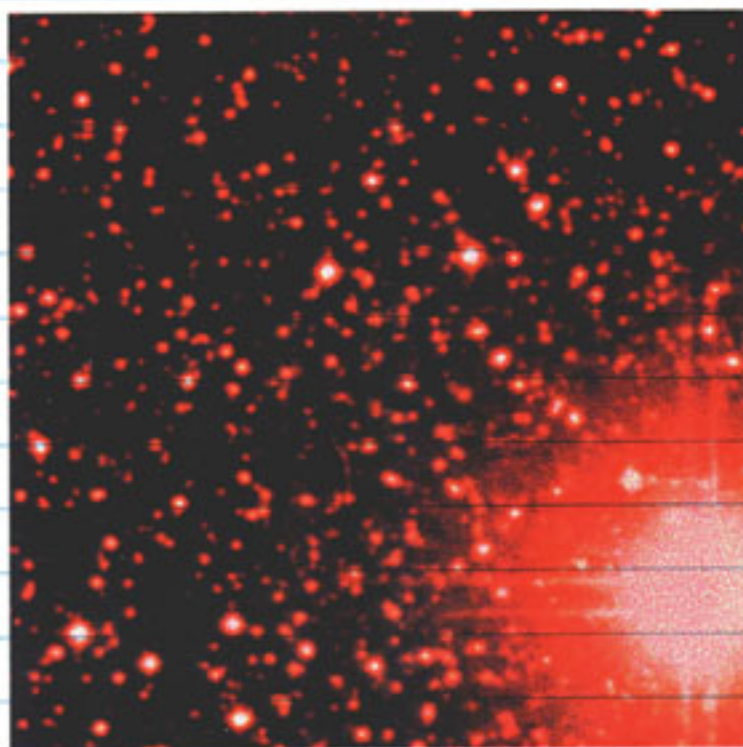
$$M_{V_A} = 7.5$$

$$M_{V_B} = 8.5$$

1951

DSS1

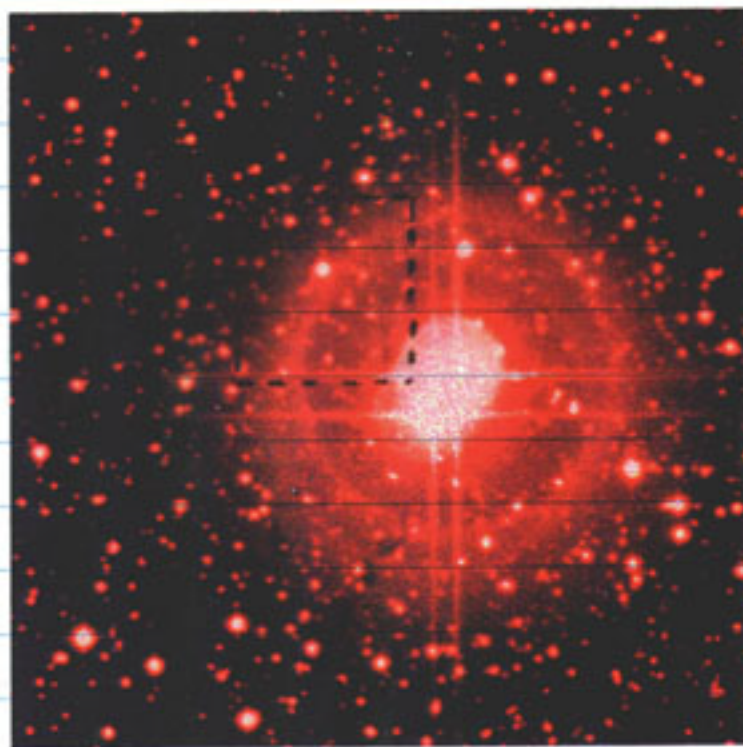
8' x 8'



1991

DSS2

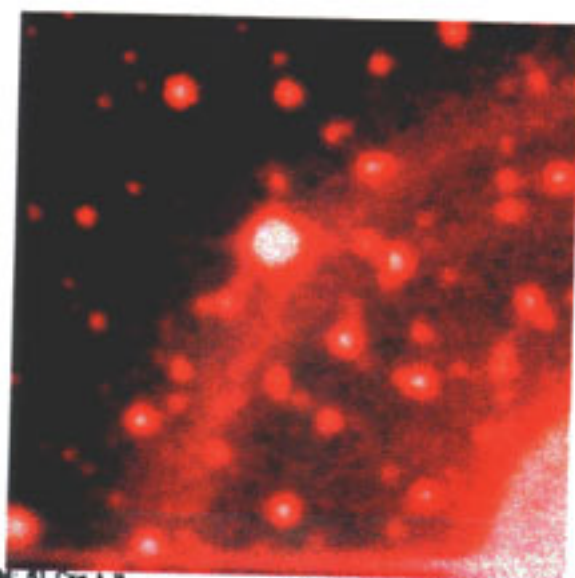
8' x 8'



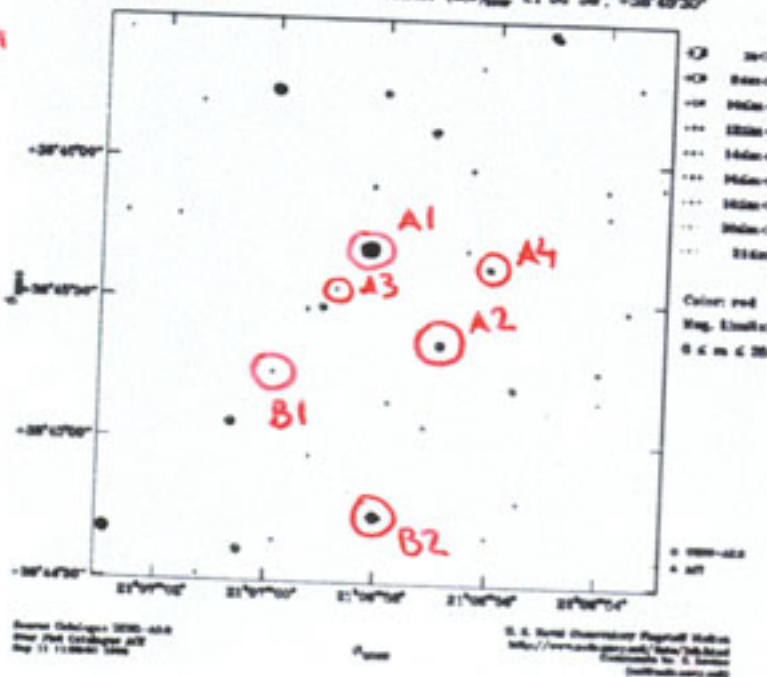
← A
← B

61 Cyg A/B - events -

2'x2'
DSS2



Field: 61 Cyg A/B Center (J2000) 21°00'58", -38°49'20"



61 Cyg A

τ_{sim}

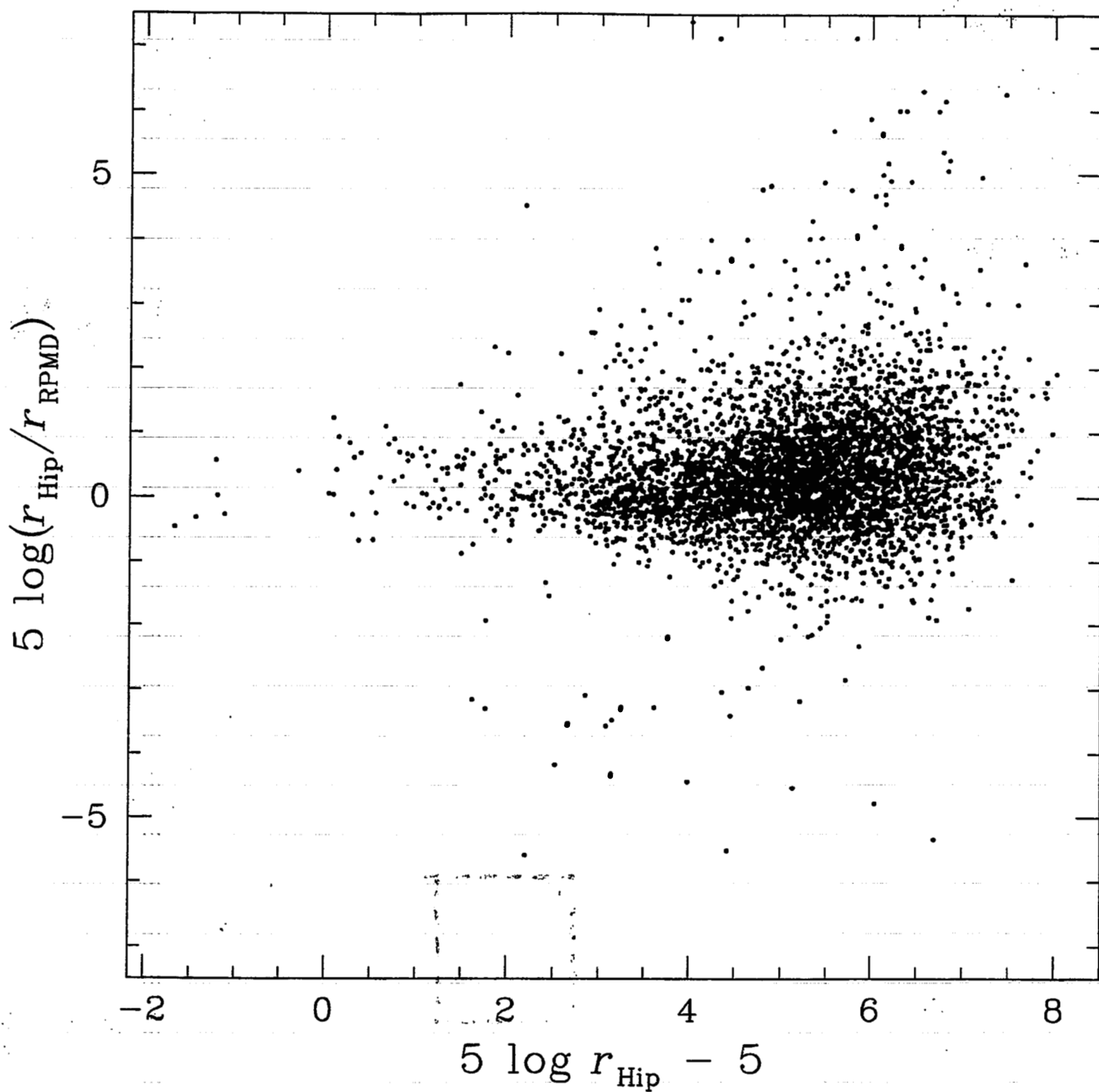
A1	2012	0.1
A2	2008	11
A3	2012	200
A4	2009	290
V		
11	10.9	
12	16.1	
13	17.3	
14	15.3	

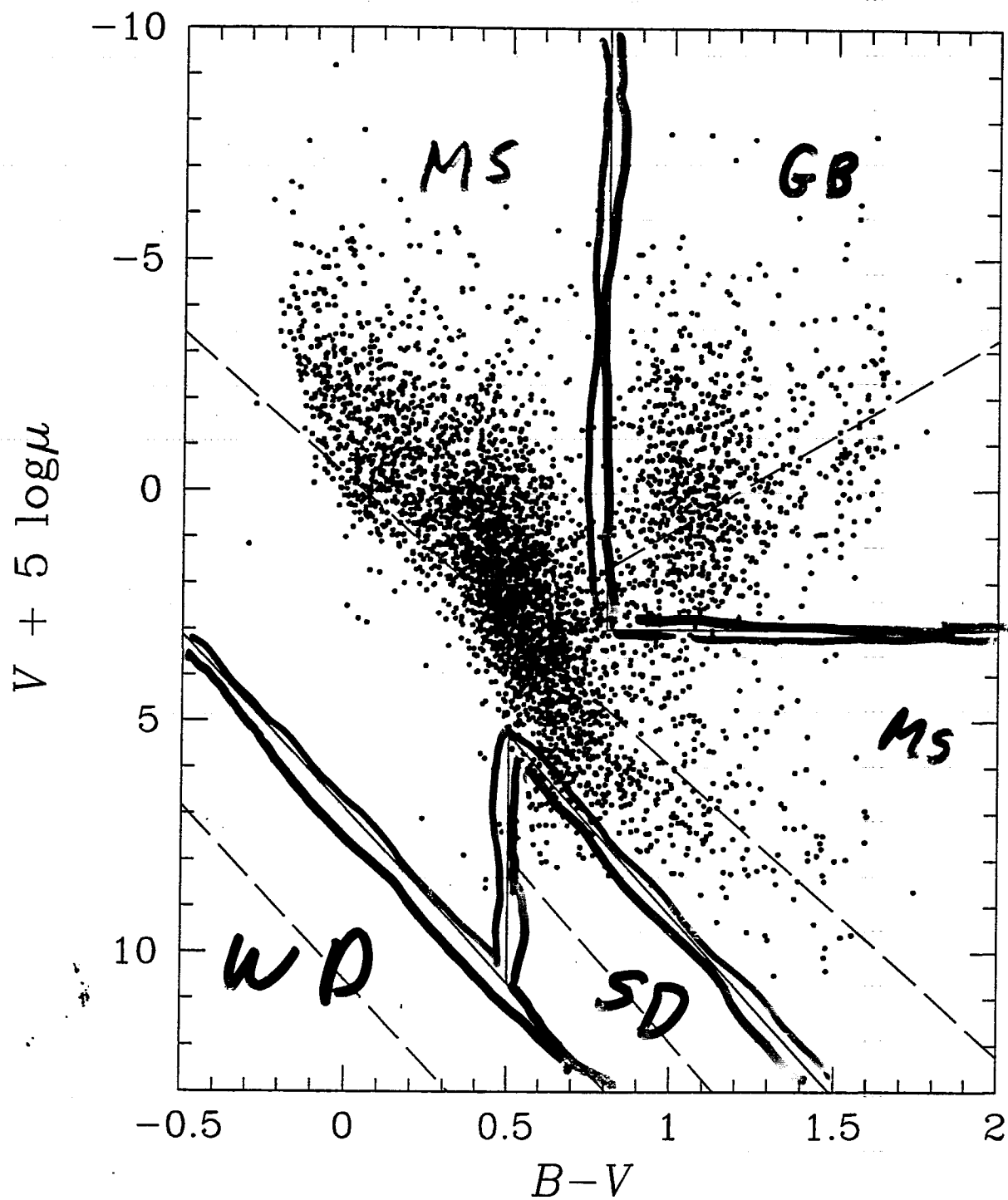
61 Cyg B

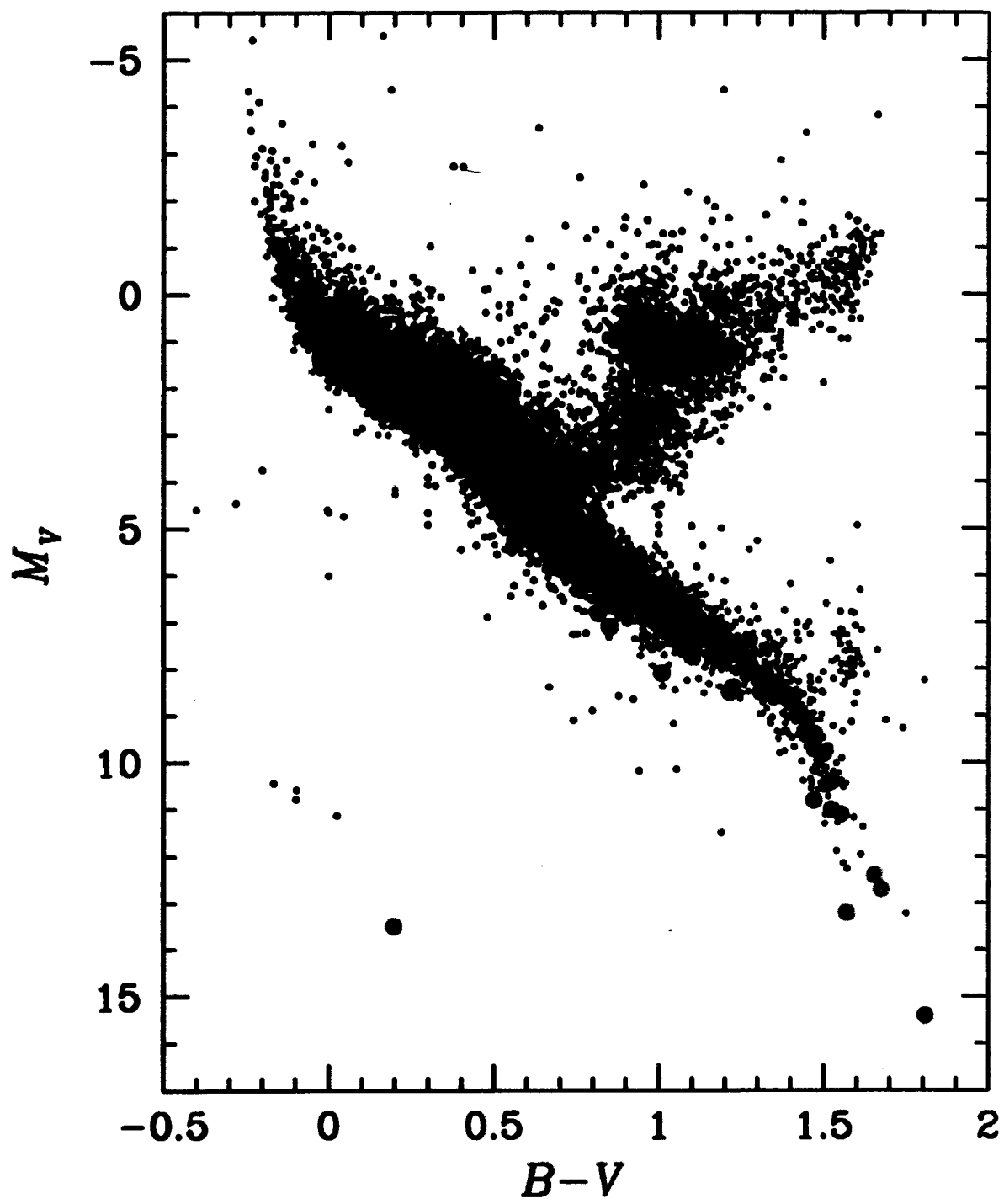
τ_{sim}

B1	2013	4
B2	2006	130
V		
B1	18.4	
B2	16.0	

DISTANCE ERRORS







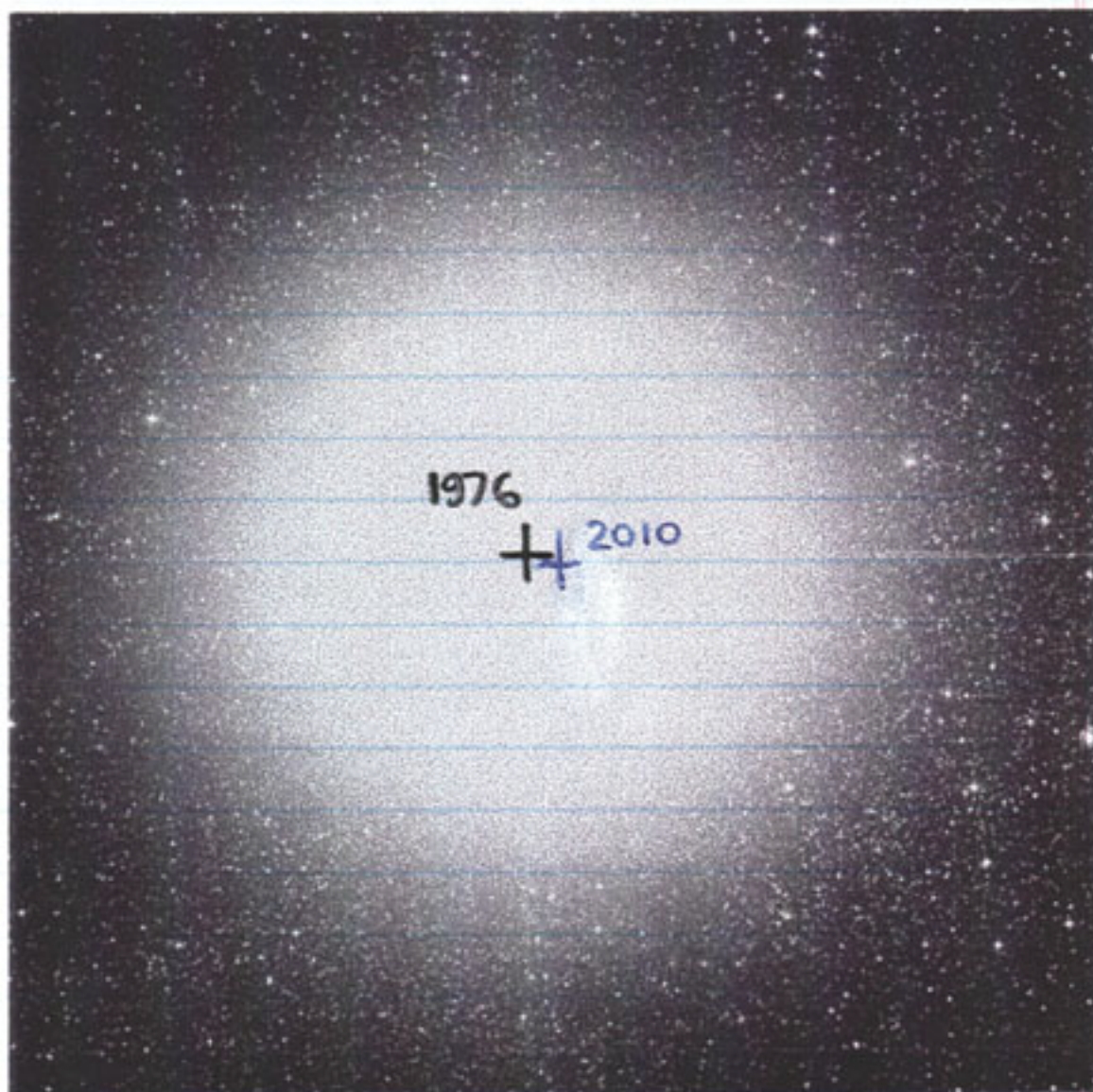
α Cen

$$V = -0.1$$

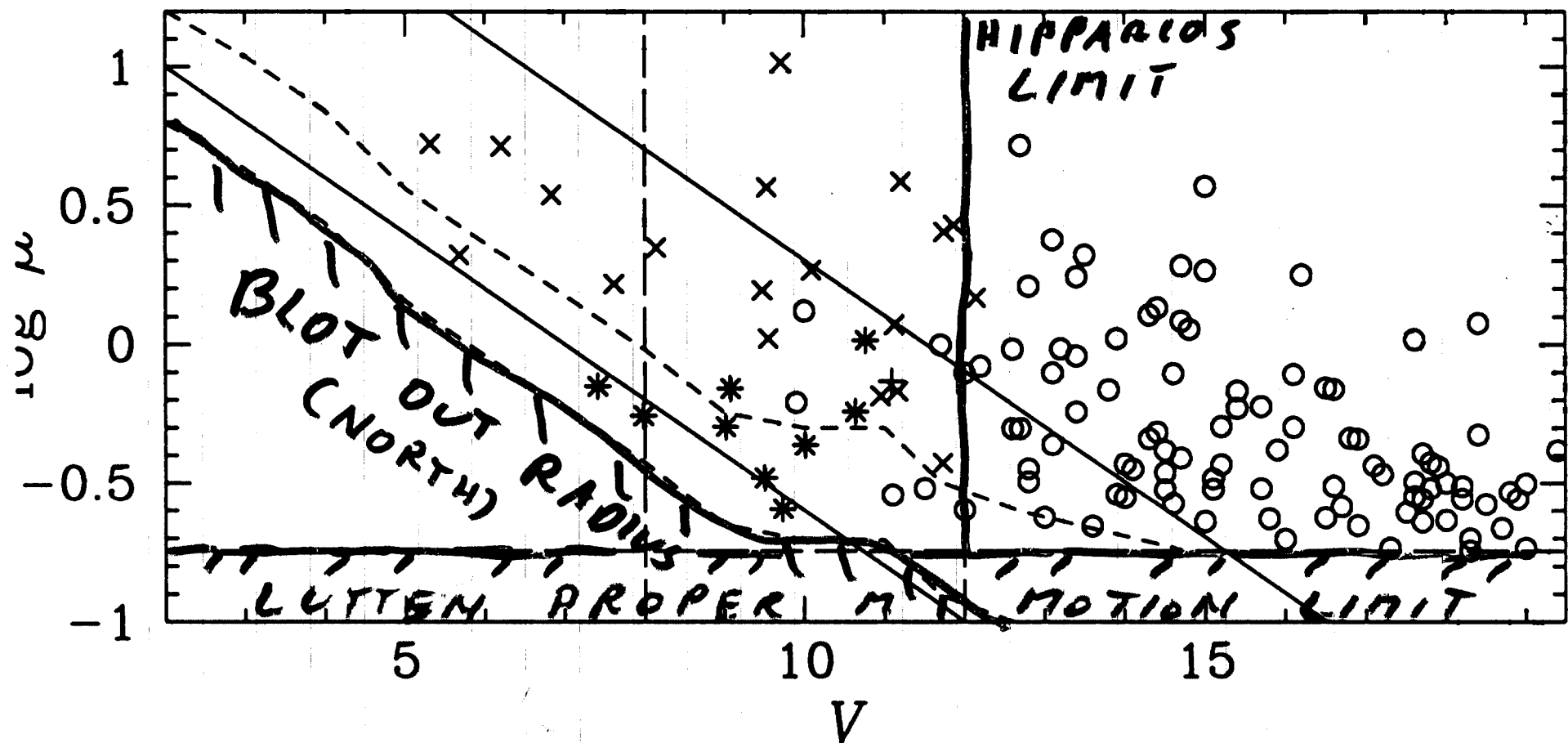
$$\mu = 3.7''/\text{yr}$$

$$d = 1.3 \text{ pc}$$

1976



60' x 60'



x HIPPARCOS
 + ACT
 o LUYTEN

red clustering 4 AXP (negative)
52 63

299-0168

ret masses in 5, 5-2 - 1.12

ret the potassium direct second AC from stars

ret black hole
big

place negative times...
default red.

$$\left(\frac{26M}{c}\right)^{3/2} \frac{D}{a^{5/2}}$$

$$2^{1/2} 8^{-5/2}$$

$$2^{1/2} 2^{-5/2} 4^{-5/2}$$

$$2^{1/2} 2^{-15/2} 2^{-6}$$

$$\frac{86M}{c}$$

$$E = \frac{wa}{2c^2} = \frac{wa}{2ac} \quad X = \frac{86M}{c}$$

$$8^{1/2} \left(\frac{GM}{c^2}\right)^{3/2} \frac{D}{a^{5/2}}$$

$$\frac{wa}{c^2}$$

$$wa = \frac{V}{a}$$

$$V^2 = \frac{G(2M)}{(2a)^2} = \frac{GM}{2a^2}$$

$$V = \sqrt{\frac{GM}{2a}}$$

$$w = \sqrt{\frac{GM}{2a^3}}$$

$$a = \frac{86M}{c} \times \frac{D}{a^{3/2}}$$

$$\frac{\left(\frac{GM}{2a^3}\right)^{1/2} \frac{4(86M)}{c^2}}{2ac}$$

$$\left(\frac{26M}{c}\right)^{3/2} \frac{D}{a^{5/2}}$$

$$\left(\frac{26M}{c}\right)^{3/2} \left(\frac{86M}{c^2}\right)^{-5/2} D^{-3/2} \times^{-3/2}$$

$$E = 64 \left(\frac{6M}{c}\right)^{-1} D^{-3/2}$$

	t sim real	HIP #	RA 1991.25	DEC	V or VT	1=V B-V	mu tot	mu pa	M_V or Mass	d(pc)	
1	9.07	104214	21 6	50.8350	+ 38 44	29.380	5.200	1 1.069	5.2807	52	7.5 0.51 3.5 SD
2	3.06	90959	18 33	17.8712	+ 22 18	55.449	9.016	0 1.181	0.5052	200	7.2 0.75 23.4 MS
3	3.19	106122	21 29	46.4600	+ 45 53	37.083	7.986	0 0.759	0.5531	50	5.6 0.94 29.8 MS
4	3.65	57367	11 45	39.2635	- 64 50	26.427	11.867	0 0.196	2.6876	97	13.5 0.60 4.6 WD
5	3.98	104217	21 6	52.1924	+ 38 44	3.890	6.208	0 1.309	5.1724	53	8.5 0.43 3.5 SD
6	4.88	86214	17 37	4.2404	- 44 19	0.968	10.940	1 1.655	1.1765	217	12.4 0.22 5.0 MS
7	7.23	28445	6 0	21.3792	+ 31 25	50.855	9.505	0 0.930	0.3297	155	6.2 0.86 46.1 MS
8	9.07	73734	15 4	19.2795	+ 60 23	2.956	11.000	1 1.500	0.6786	285	9.8 0.53 17.6 MS
9	10.95	104214	21 6	50.8350	+ 38 44	29.380	5.200	1 1.069	5.2807	52	7.5 0.51 3.5 SD
10	12.55	70890	14 29	47.7474	- 62 40	52.867	11.010	1 1.807	3.8530	281	15.4 0.11 1.3 MS
11	12.55	85523	17 28	39.4569	- 46 53	34.986	9.380	1 1.553	1.0501	147	11.1 0.36 4.5 MS
12	15.74	64965	13 18	57.0885	- 3 4	16.904	10.840	1 1.009	0.6517	258	8.1 0.46 35.9 SD
13	36.53	57367	11 45	39.2635	- 64 50	26.427	11.867	0 0.196	2.6876	97	13.5 0.60 4.6 WD
14	43.33	74234	15 10	13.5770	- 16 27	15.521	9.440	1 0.850	3.6815	196	7.1 0.55 29.7 SD
15	46.01	98906	20 5	3.3563	+ 54 26	11.144	11.980	1 1.524	1.4724	232	11.0 0.23 15.8 SD
16	57.96	87937	17 57	48.9655	+ 4 40	5.837	9.540	1 1.570	10.3577	356	13.2 0.12 1.8 SD
17	60.93	76074	15 32	13.8455	- 41 16	23.108	9.310	1 1.524	1.5636	229	10.4 0.46 5.9 MS
18	66.64	33582	6 58	38.3423	- 0 28	44.391	9.075	0 0.579	0.6930	151	4.9 0.80 68.4 SD
19	74.25	114622	23 13	14.7435	+ 57 10	3.498	5.570	1 1.000	2.0952	82	6.5 0.81 6.5 MS
20	78.38	61629	12 37	53.1966	- 52 0	5.580	10.767	0 1.470	1.0347	272	10.8 0.42 9.7 MS
21	85.33	27207	5 46	1.5287	+ 37 17	9.195	7.417	0 0.833	0.7050	136	5.9 0.91 20.6 MS
22	112.30	74926	15 18	39.2706	- 18 37	32.607	10.643	0 1.214	0.5713	128	8.5 0.62 26.2 MS
23	124.81	70890	14 29	47.7474	- 62 40	52.867	11.010	1 1.807	3.8530	281	15.4 0.11 1.3 MS
24	130.82	104217	21 6	52.1924	+ 38 44	3.890	6.208	0 1.309	5.1724	53	8.5 0.43 3.5 SD
25	137.84	70890	14 29	47.7474	- 62 40	52.867	11.010	1 1.807	3.8530	281	15.4 0.11 1.3 MS
26	144.99	102923	20 51	6.5386	+ 7 1	40.380	10.014	0 0.900	0.4333	147	6.6 0.61 48.3 SD
27	181.83	48336	9 51	8.9608	- 12 19	34.728	10.093	0 1.446	1.8487	142	9.4 0.35 13.7 SD
28	184.69	87937	17 57	48.9655	+ 4 40	5.837	9.540	1 1.570	10.3577	356	13.2 0.12 1.8 SD
29	187.52	105090	21 17	17.7112	- 38 51	52.468	6.690	1 1.397	3.4549	251	8.7 0.60 3.9 MS
30	197.45	25878	5 31	26.9506	- 3 40	19.712	8.144	0 1.474	2.2277	160	9.4 0.56 5.7 MS
31	202.43	104214	21 6	50.8350	+ 38 44	29.380	5.200	1 1.069	5.2807	52	7.5 0.51 3.5 SD
32	215.48	79537	16 13	49.4874	- 57 34	1.492	7.530	1 0.815	1.6491	211	6.8 0.58 13.7 SD
33	219.01	101369	20 32	43.0692	+ 19 31	38.648	11.630	1 0.880	0.3738	192	6.7 0.60 98.9 SD
34	256.25	87101	17 47	46.1616	- 9 36	16.619	9.732	0 0.672	0.2546	215	4.9 0.81 94.3 SD
35	274.12	26857	5 42	8.0726	+ 12 29	35.358	11.560	1 1.675	2.5423	128	12.7 0.19 5.8 MS
36	289.69	104214	21 6	50.8350	+ 38 44	29.380	5.200	1 1.069	5.2807	52	7.5 0.51 3.5 SD
A1	16.140	368588	18 24	50.7708	+ 6 56	54.791	11.092	0 1.224	0.7359	273	8.4 0.62 35.0 MS

RA USNO	DEC USNO	VT usno	B-Vusno	field	d2000(") l min	beta(mas)	ACT?	Sp	Alternative name	
21 6 58.2289	+ 38 45 41.144	10.9	0.61	0	66.2	12.524	3064 N	K5V	61 Cyg A	1
18 33 17.6028	+ 22 18 46.648	15.9	0.10	392	5.2	10.160	456 Y	K4V	V774 Her	2
21 29 47.3657	+ 45 53 45.366	16.4	0.96	188	7.7	13.904	366 Y	G8V	HD 204814	3
11 45 48.9681	- 64 50 33.737	18.1	0.90	94	38.8	14.444	738 N	DC:	GJ 440	4
21 6 59.9455	+ 38 45 14.227	18.4	0.61	286	69.6	13.455	636 N	K7V	61 Cyg B	5
17 37 2.5204	- 44 19 21.955	13.6	0.96	279	17.7	14.921	2022 no V	M5	GJ 682	6
6 0 21.6242	+ 31 25 44.733	16.9	1.19	307	4.0	12.195	262 Y	K2	HD 250047	7
15 4 17.8079	+ 60 23 5.376	16.7	0.49	100	5.2	7.673	520 no V	M:	Ross 1051	8
21 6 56.9380	+ 38 45 20.654	16.1	0.92	286	41.8	7.881	3686 N	K5V	61 Cyg A	9
14 29 39.5826	- 62 40 42.810	17.1	1.15	98	23.4	6.085	1360 N	M5Ve	Alpha Cen C	10
17 28 40.8504	- 46 53 50.640	13.8	1.28	278	12.2	11.152	3401 no V	K5	GJ 674	11
13 18 56.1992	- 3 4 20.843	13.5	0.49	618	8.3	12.565	1136 N	K5	Ross 484	12
11 45 46.1254	- 64 50 29.288	17.7	0.90	94	20.4	7.523	2805 N	DC:	GJ 440	13
15 10 11.9934	- 16 28 29.088	14.5	0.57	804	44.8	12.162	1862 N	K0V:	HD 134440	14
20 5 1.0872	+ 54 25 56.104	18.5	0.73	144	12.0	8.159	243 no V	M3	V1513 Cyg	15
17 57 47.9718	+ 4 43 0.771	18.4	0.30	570	84.9	9.182	1286 N	sdM4	Barward Star	16
15 32 11.8050	- 41 16 47.515	16.4	0.96	329	20.0	12.600	3261 no V	M0	GJ 588	17
6 58 38.7630	- 0 28 53.972	15.7	0.61	602	5.4	7.762	863 Y	G0	HD 51754	18
23 13 18.7267	+ 57 10 12.543	17.0	0.84	149	15.7	7.189	4364 N	K3Vvar	HD 219134	19
12 37 50.9118	- 52 0 5.946	18.4	1.02	218	12.1	11.646	974 Y	M3	GJ 479	20
5 46 2.3560	+ 37 17 0.795	17.5	0.80	253	6.9	9.569	1349 Y	K0V	HD 38230	21
15 18 40.0115	- 18 37 39.531	16.9	0.64	582	7.6	13.162	1109 Y		BD-18 4031	22
14 29 38.1235	- 62 40 35.971	17.7	0.74	98	34.7	8.972	3341 N	M5Ve	Alpha Cen C	23
21 6 58.0435	+ 38 44 44.125	16.0	0.41	286	34.9	8.489	9655 N	K7V	62 Cyg B	24
14 29 36.0807	- 62 40 40.489	17.5	0.80	98	47.6	12.619	3885 N	M5Ve	Alpha Cen C	25
20 51 6.7923	+ 7 1 35.526	18.0	0.57	577	2.4	5.394	464 Y	K3	BD+06 4665	26
9 51 10.0195	- 12 19 57.922	16.6	0.30	730	11.8	6.295	2040 N	M0	SAO 155530	27
17 57 47.3607	+ 4 44 5.206	16.5	0.73	570	150.0	12.475	5503 N	sdM4	Barward Star	28
21 17 13.3809	- 38 51 59.527	16.0	1.28	342	22.3	5.737	10139 N	M1/M2V	AX Mic	29
5 31 27.6228	- 3 40 56.323	18.7	0.45	659	18.6	8.237	3056 N	M1V	HD 36395	30
21 6 58.8332	+ 38 45 32.300	17.3	1.16	286	66.8	12.553	8266 N	K5V	61 Cyg A	31
16 13 47.7512	- 57 34 27.256	18.6	1.18	137	14.9	8.989	1414 N	K0V	HD 145417	32
20 32 42.9410	+ 19 31 31.269	18.4	0.49	456	4.3	11.585	235 no V	K3	MU Del	33
17 47 46.0652	- 9 36 19.907	16.7	0.84	750	1.5	5.297	596 Y	G0	HD 161770	34
5 42 11.0492	+ 12 29 2.596	18.8	0.61	479	32.3	12.686	1170 N	M5	V1352 Ori	35
21 6 56.0660	+ 38 45 37.573	15.3	0.57	286	46.8	8.339	15873 N	K5V	61 Cyg A	36
18 24 49.8697	+ 6 56 55.677	18.7	0.73	571	7.0	9.475	161 Y (only)			

CONCLUSIONS

SIM APPLICATIONS

BULGE MASS FUNCTION

WHITE DWARFS

NEUTRON STARS

BLACK HOLES

BROWN DWARFS

MASSES OF NEARBY STARS

FUTURE APPLICATIONS

PLANETS

BINARIES

⋮